Multi-seasonal measurements of the ground-level atmospheric ice-nucleating particle abundance on the North Slope of Alaska

Aidan D. Pantoya[1], Stephanie R. Simonsen[2], Elisabeth Andrews[3], Ross Burgener[4], Christopher J. Cox[5], Gijs de Boer[6], Bryan D. Thomas[4], and Naruki Hiranuma[2]

[1]West Texas A&M University, College of Engineering, Canyon, 79016, USA

[2]West Texas A&M University, Department of Life, Earth, and Environmental Sciences, Canyon, 79016, USA

[3]Cooperative Institute for Research in Environmental Sciences, University of Colorado Boulder, Boulder, 80309, USA

[4]Global Monitoring Laboratory, National Oceanic and Atmospheric Administration (NOAA), Barrow, 99723, USA

[5]Physical Sciences Laboratory, National Oceanic and Atmospheric Administration (NOAA), Boulder, 80305, USA

[6]Environmental Sciences Science and Technologies Department, Brookhaven National Laboratory, Upton, 11973, USA

Correspondence to: Naruki Hiranuma (nhiranuma@wtamu.edu)

ABSTRACT

Atmospheric ice-nucleating particles (INPs) are an important subset of aerosol particles that are responsible for the heterogeneous formation of ice crystals. INPs modulate arctic cloud phase (liquid vs. ice), resulting in implications for radiative feedbacks. The number of arctic INP studies investigating specific INP episodes or sources has recently increased. However, existing studies are based on short-duration field data and long-term datasets are lacking. Continuous, long-term measurements are key to determining the abundance and variability of ambient arctic INPs and for constraining aerosol-cloud interactions, for example, to verify and/or improve simulations of mixed-phase clouds. Here, we present a new long-duration INP dataset from the Arctic: two years of predominantly immersion mode INP concentrations (n_{INP}) measured continuously at the National Oceanic and Atmospheric Administration's Barrow Atmospheric Baseline Observatory on the North Slope of Alaska. A portable ice nucleation experiment chamber (PINE-03), which simulates adiabatic expansion cooling, was used to directly measure the ground-level INP abundance with an approximately 12-minute time resolution from October 2021 to December 2023. We document PINE-03 n_{INP} measurements, as well as estimated ice nucleation active surface site density (n_s), over a wide range of heterogeneous freezing temperatures from −16 to −31 °C from which we introduce new season-specific parameterizations suitable for modeling mixed-phase clouds. Collocated aerosol and meteorological data were analyzed to assess the correlation between ambient n_{INP}, air mass origin region, and meteorological variability. Our findings suggest

(1) very high freezing efficiency of INPs across the measured temperatures ($n_s \approx 2 \times 10^8 - 10^{10}$ m^{-2} for from -16 to -31 °C), which is a factor of $10 - 1000$ times greater efficiency as compared to that found in the previous mid-latitude INP measurements in autumn using the same instrument; (2) surprisingly high n_{INP} (≥ 1 L-1 at -25 °C) for the examined temperatures throughout the year that were not measured by PINE-03 at other sites; and (3) high n_{INP} in spring, possibly related to arctic haze episodes. Relatively low concentrations of aerosol surface area and contrasting high INP concentrations at BRW relative to mid-latitude sites are the possible reasons for the observed high freezing efficiency.

1. INTRODUCTION

Ice formation in the atmosphere is facilitated by ice-nucleating particles (INPs) through heterogeneous freezing (Hoose and Möhler, 2012) by reducing the activation energy required to induce the release of latent heat, thereby triggering spontaneous ice growth (Vali et al., 2015). Below ≈ -35 °C, freezing of supercooled water droplets can take place homogeneously (Koop and Murray, 2016). At warmer sub-zero temperatures, several heterogeneous freezing mechanisms are important, including immersion freezing, which is a dominant ice formation pathway in mixed-phase clouds (hereafter referred to as MPCs) (Hande and Hoose, 2017; Westbrook and Illingworth, 2011).

In the Arctic, MPCs are ubiquitous, dominating features of the low cloud fraction (Morrison et al., 2012) and radiative balance (e.g., Shupe and Intrieri, 2004). They are observed in a variety of conditions and in all seasons (e.g., Shupe et al. 2010; 2011; 2013). INPs can act as cloud-destroying agents in MPCs. For example, model sensitivity studies indicate that MPC lifetime is strongly sensitive to INP concentration (n_{INP}) (Solomon et al., 2018) despite the fact that n_{INP} is several orders of magnitude smaller than concentrations of cloud condensation nuclei (CCN) (Lee et al., 2023; Mamouri and Ansmann, 2016). The forcing and feedback mechanisms associated with aerosols and clouds remain uncertain (Kanji et al., 2017; Solomon et al., 2009). Murray et al. (2021) postulate that, in the Arctic, MPCs could decrease due to positive feedback with atmospheric INPs, supported by reduced snow and ice coverage enhancing INP emissions from exposed terrestrial surfaces, or even thermokarst landforms (Barry et al., 2023).

Arctic INPs have been reported in several past studies, in particular from the North Slope of Alaska (NSA), as summarized in Appendix A. Fountain and Ohtake (1985) found mean INP abundance of ≈ 0.2 L^{-1} at -20 °C at the surface there from August 1978 to April 1979. Prenni et al. (2007) measured similar n_{INP} from aircraft, with a mean of ≈ 0.2 L^{-1} in deposition and condensation freezing modes over ≈ -8 °C to -28 °C. Elevated n_{INP} (up to ≈ 40 L^{-1}) were measured in the temperature range between ≈ -14 °C and -30 °C during the aircraft measurements along the NSA coast by Sanchez-Marroquin et al. (2023). While the authors found the INP source identification challenging (i.e., terrestrial, permafrost, maritime, biogenic, and/or a combination of any), their complementary aerosol particle composition and back trajectory results implied that local and remote emissions and sinks of INP played an important role in the n_{INP} variability.

70   Several aircraft-based studies documented that greater n_{INP} leads to more ice in arctic clouds. For example, Rogers et al. (2001) reported mean n_{INP} of up to 57 L^{-1} in the examined temperature range between −10 °C and −30 °C during May 1998. High INPs in the NSA region were reported in a more recent research vessel study in the Chukchi Sea (Inoue et al., 2021). Based on offline freezing assay analysis, the authors measured up to ≈ 100 L^{-1} in the temperature range

75   between −7.5 °C and −29.5 °C. The observed high INP abundance during cold-air outbreak events was attributed to ocean mixing and associated sea spray emission of ice nucleation active organic substances. Over land, INP studies report ambient mineral dust to be a significant source of arctic INPs. For instance, high INP episodes were also seen in an Iceland study (> 100 L^{-1} at −26 °C; Sanchez-Marroquin et al. 2020) and from southern Alaska (≈ 6 L^{-1} at −26 °C; Barr et al. 2023),

80   suggesting the importance of high latitude dust and other local terrestrial INP sources.

       In contrast, Creamean et al. (2018a) reported lower n_{INP} at Oliktok Point, Alaska, about 250 km to the ESE of Utqiaġvik (formerly known as Barrow), Alaska. During March-May, 2017, they measured n_{INP} up to ≈ 4.4 x 10^{-2} L^{-1} for aerosol particles in the diameter range between 0.15 to 12 μm over the examined freezing temperatures. Creamean et al. (2018a,b) also found that the

85   composition of aerosols from their study region varied, but it typically included terrestrial and/or maritime materials. Their source analysis postulates that bubble bursting and bacteria or fragments of marine organisms can act as the INP source from ice-free open water. Similarly, a ship-based study examining sea spray aerosol as the INP source over the central Bering Sea in summer 2012 found low abundance, up to ≈ 2.0 x 10^{-2} L^{-1} from −12 °C to −20 °C (DeMott et al., 2016). Low

90   ambient n_{INP} has been found in arctic regions farther from Alaska, too. Creamean et al. (2022) reported < 0.1 L^{-1} at −25 °C during the Multidisciplinary drifting Observatory for the Study of Arctic Climate (MOSAiC) expedition in the Central Arctic (September 2019 − October 2020). Similar to the MOSAiC finding, the offline freezing assay performed by Welti et al. (2020; W20 hereafter) showed n_{INP}(−28°C) of ≲ 0.2 L^{-1} from the PS 106 arctic expedition in the vicinity of

95   Svalbard, Norway (May − July 2017). Continental dust during winter and marine biota from ice-free open water in summer were identified as the potential INP sources (Creamean et al., 2022; Irish et al., 2019a,b; Creamean et al., 2019; C19 hereafter).

       Compiling eight previous INP studies from Alaskan, Canadian, and European arctic regions covering a wide range of freezing temperatures, Wilbourn et al. (2023) summarize

100   abundance as spanning seven orders of magnitude (≈ 10^{-5} to 70 L^{-1}). Because the INP abundance

is so variable, and most data thus far have been limited to brief campaigns, it is important to develop and analyze INPs statistically based on continuous, long-term, and finely-resolved measurements (Murray et al., 2021). This study reports on seasonality in the abundance of INPs activated at conditions relevant to mixed-phase clouds (predominantly immersion mode) using a single instrument, a Portable Ice Nucleation Experiment (PINE) chamber version 03 (PINE-03 hereafter). The PINE-03 was installed on the NSA near Utqiaġvik for multi-seasonal INP monitoring. In addition to a statistical analysis of n_{INP}, we combine the measurements with observatory data there to construct a parameterization for heterogeneous freezing efficiencies of ambient aerosols (i.e., n_{INP} scaled to aerosol abundance).

2. DATA & METHODS

A. STUDY SITE AND PERIOD

Observations were made at the National Oceanic and Atmospheric Administration (NOAA) Barrow Atmospheric Baseline Observatory (71.32° N, 156.61° W, "BRW" hereafter), ~ 6 km northeast of the town of Utqiaġvik. Our observing period began October 2021 and continued until May 2024 as the field component of Examining INP at NSA (ExINP-NSA), covering nearly 32 months. Here, we utilize data acquired from mid-October 2021 through December 2023. We note that any data gaps pertain to the PINE-03 system maintenance, as required every $3-4$ months (see Wilbourn et al., 2024; SI Sect. S5). The maintenance was also conducted immediately after we observed and flagged the PINE-03 operational issues. The most common problems include an OPC malfunction, diaphragm pump filter replacement, or LabView data acquisition console disconnection. During ExINP-NSA, we rarely observed such issues (41 out of 1506 operations, 2.7%), and PINE-03 ran reliably with scheduled maintenance periods. Operational flagging was assessed every cycle during measurements.

Although measurements at BRW are made over open tundra, there are large lagoons and numerous lakes in the vicinity, and the Arctic Ocean is less than 3 km to the north and east. Because of its proximity to these bodies of water and the prevailing easterlies from the Beaufort Sea, BRW is perhaps best characterized as having an arctic maritime climate modulated by nearby sea ice conditions, but is also influenced by episodic atmospheric advection from the North Pacific (e.g., Cox et al., 2012, 2017). The BRW observatory was chosen for ExINP-NSA to collocate with NOAA's atmospheric baseline measurements, which include aerosol optical, microphysical and

chemical properties, and meteorology. To complement the current BRW capabilities, we experimentally characterized INP abundance in association with the physicochemical properties of ambient aerosols. The findings are described throughout Sect. 3. BRW is equipped with well-characterized laminar flow stack inlets, and the air intake is about 12 m above ground level (AGL, Andrews et al., 2019). Moreover, at the beginning of the field campaign, we conducted a complementary characterization of aerosol transmission efficiency through the inlet, and the result is reported in the Supplementary Information (SI) Sect. S1. No corrections for particle losses or sampling conditions are applied to any aerosol data used in this report (see SI Sect. S1).

B. INP CONCENTRATION MEASUREMENT

The PINE-03 system measures ambient n_{INP} *in situ* using a simulated adiabatic expansion cooling method (Möhler et al., 2021). This system is a commercialized product, resulting in consistent operation amongst studies (Möhler et al., 2021; Knopf et al., 2021; Lacher et al., 2024; Wilbourn et al., 2024) compared to traditional INP monitoring devices that are typically custom-built by individual scientists. Besides relatively high measurement time resolution (less than or equal to 12 min), the advantages of PINE-03 include (1) no substantial artifacts (e.g., no ice off of the vessel wall); (2) remote operation capability with minimum in-person maintenance or supervision requirements; and (3) fast turnover time to scan freezing temperatures in a wide range (Wilbourn et al., 2024).

The PINE-03 system operates by a combination of "flush", "expansion", and "refill" modes, cycling approximately every $5 - 12$ minutes. During the flush mode, ambient air is actively dried through a set of two Perma Pure dryers and is injected into the 10 L volume chamber with a flow rate of 2 LPM for 10 minutes. In the subsequent expansion mode, sample gas temperature and pressure are reduced with $3\,\mathrm{L\,min^{-1}}$ of pump flow rate to $800\,\mathrm{hPa}$ in the vessel to supersaturation with respect to both ice and water. This simulated adiabatic expansion typically lasts about one minute and triggers ice nucleation if INPs are present in the sample. An optical particle counter (OPC; fidas-pine; Palas GmbH) deployed downstream of the chamber then detects particles exiting the chamber. Based on the optical size (typically $> 10\,\mu\mathrm{m}$ in diameter), ice crystals can be separated from other particles (i.e., interstitial aerosols and/or water droplets) and counted as predominantly immersion mode INPs. During the refill mode, filtered air is injected into the chamber for approximately a minute to precondition the vessel for the next run cycle.

To harmonize datasets collected with different time intervals, the INP dataset was processed by averaging over 6 hours and synchronized to the same time scales following the previous PINE-03 study led by Wilburn et al. (2024). In our typical chamber operation, the air gas set-point temperature is changed between −10 and −31 °C. The time resolution of such a temperature ramp was approximately 2 hours, and thereby the 6-hour time-averaged PINE-03 data represent n_{INP} from three temperature ramps. Single PINE-03 'operation' typically lasts a day until daily maintenance is performed. Therefore, a set of multiple temperature ramps was acquired daily. The PINE-03 was cleaned daily by flushing filtered ambient dry air through the chamber until no particles were detected. We followed other long-term chamber maintenance protocols as described in Wilbourn et al. (2024).

The highest freezing temperature for detecting INPs at NSA was −10.4 °C based on the original data acquisition time resolution. The PINE-03 system has a temperature uncertainty of ± 1.5 °C. The total effective sampling volume is a combination of the chamber size, the number of sampling cycles that are averaged, and the pressure to which the chamber is filled. A detection limit of PINE-03 is 0.2 L^{-1} for individual expansion, which corresponds to a single INP detection per air volume assessed in a single expansion ($\approx$ 3.4 L on average), and 0.02 L^{-1} on a 6-hour time average basis, allowing summed air volume assessment specific to the ExINP-NSA conditions. With this detection limit, a temperature-dependent Poisson error analysis was carried out in the field, which verified the statistical validity of the PINE-03 data below −16 °C (see SI Sect. S2). Nonetheless, due to this upper temperature limit, we note that observed INPs do not necessarily represent INPs in near-surface clouds. Further details of the working principle of the PINE-03 system, as well as its calibration protocol and data, can be found in Möhler et al. (2021) and Wilbourn et al. (2024).

C. Aerosol Data

1. Aerosol Number Concentration

Aerosol number concentrations (n_{aer}) were measured at BRW with a condensation particle counter (CPC; model 3010, TSI Inc.). The n_{aer} was used to indicate total aerosol particle abundance over the study period and to compute the INP-activated fraction ($IAF = n_{INP}(T)/n_{aer}$). In addition, another CPC (model 3772, TSI Inc.) was operated at the adjacent U.S. Department of Energy (DOE) Atmospheric Radiation Measurement (ARM) program site as part of the NSA Aerosol Observing

System. Both the 3010 and 3772 CPC have a 10 nm minimum cut size. Over our $\approx$ 2-year study period, similar n_{aer} was measured by the BRW-CPC (median of 156.3 cm^{-3}) and the ARM-CPC (179.0 cm^{-3}) for non-screened datasets. Although the BRW-CPC reads slightly lower than ARM-CPC based on 6-hour time-averaged medians, the Pearson correlation coefficient, r, between two CPC datasets is high ($r \approx 0.9$). All n_{aer} presented here are from the BRW-CPC. To make all data from instruments that have different sampling times comparable, all online datasets discussed in this study were averaged over 6-hour periods.

2. SURFACE AREA CONCENTRATION

We estimate aerosol surface area concentration (S_{aer}) at volume standard temperature and pressure (273.15 K and 1013.25 hPa) using aerosol scattering coefficients measured by an integrating nephelometer (Model 3563, TSI Inc.). Aerosol scattering coefficients from the nephelometer are reported in units of inverse megameters (Mm^{-1}). The application of nephelometer data to calculate the aerosol surface areas has been demonstrated in prior studies in marine conditions (DeMott et al., 2016; Wilbourn et al., 2024). Aerosol scattering coefficients at three wavelengths (450, 550, and 700 nm) were continuously measured by the nephelometer, which was operated under low humidity conditions (< 40 % relative humidity). S_{aer} values are computed by scaling aerosol scattering coefficients at 450 nm (b_{sp}^{450}) by a factor of 4 and normalizing the scaled number to Q using the following equation (Moore et al., 2022):

$$S_{aer} = 4\frac{b_{sp}^{450}}{Q}, \qquad [1]$$

where Q is an effective aerosol scattering efficiency. The annual average coarse mode (i.e., PM_{10} − PM_1) Q value of 2.37 ($\pm$ 0.04 standard deviation) derived during clean marine conditions at El Arenosillo, Spain, is considered a representative Q and used in this study. More details are discussed in SI Sect. S3. We use S_{aer} to assess particle surface area and to compute ice nucleation active surface site density, $n_s(T) = n_{INP}(T)/S_{aer}$.

3. BLACK CARBON MASS CONCENTRATION

Black carbon mass concentration (m_{BC}) was estimated for the PM_{10} size range based on the Continuous Light Absorption Photometer (CLAP, Ogren et al., 2017). The CLAP is a filter-based instrument that uses Beer's law to relate the change in optical transmission through a filter caused by particle deposition to the light absorption coefficient of deposited particles. Aerosol absorption

220   coefficients from the CLAP are also reported in units of Mm^{-1}. Measured mass absorption cross-section values for freshly generated black carbon fall within a relatively narrow range of $7.5 \pm 1.2\ m^2\ g^{-1}$ at 550 nm (Bond et al., 2013). This assumption of uniform aerosol composition may introduce uncertainties in information derived from CLAP data, which represents a limitation of this study, as few natural aerosol populations have uniform composition. Here, m_{BC} ($ng\ m^{-3}$)

225   was estimated by dividing the absorption at 528 nm by the estimated mass absorbing cross-section of $7.5\ m^2\ g^{-1}$ (Zheng et al., 2018; Bond et al., 2013).

4. PARTICLE SULPHATE AND NITRATE MASS CONCENTRATION

Ambient mass concentrations of major arctic haze tracers, such as non-sea salt (nss) $SO_4^=$ and aerosol NO_3^-, were measured using filter samples of atmospheric aerosols collected at BRW for

230   subsequent ion analysis (Quinn et al., 2002; 2000; 1998). We calculated nss particle sulfate mass concentration by relating total $SO_4^=$ ion mass concentration to the mass concentration of reference species, such as sodium, in seawater ([nss $SO_4^=$] = [$SO_4^=$] − (0.252 x [Na])) (Keene et al., 1986). While both submicron and supermicron particle data are available, supermicron data availability had very limited temporal resolution (minimum 7 days, maximum 28 days). Therefore, we used

235   the submicron dataset to represent arctic haze tracers. It is worth noting that submicron $SO_4^=$ and NO_3^- were the predominant contributors to total mass of the submicron ions (a factor of $4-5$ more compared to supermicron mass where sea salt is the dominant species) for periods when both datasets were available. We also note that sampling resolution of this offline ion analysis data is much longer than 6 hours (minimum 24 h, maximum 96 h), and the sampling interval varied with

240   season. Therefore, the 6-hour time averaging protocol was not applied for this offline data, and we report the ion concentration data in its native time resolution. The filter measurements only sample when air is coming from the clean air sector (see next section).

5. AEROSOL DATA FLAGGING

NOAA's aerosol data protocol flags data as contaminated when the measured wind direction (WD)

245   is aligned with the town of Utqiaġvik (i.e., 130° < WD < 360°). Thus, aerosol data from the wind direction of Utqiagvik are automatically flagged. The clean air sector at BRW is to the east (0° < WD < 130°). The full flagging method is described in Sheridan et al. (2016). Briefly, in addition to wind direction criterion, CPC spikes, notable contamination identified by instrument mentors, and abnormally low wind speed time periods are considered in the flagging algorithm. This method

250   is consistent across NOAA observatories and varies only by clean air sector definition. NOAA provides flagging information for the aerosol data for every minute. NOAA's aerosol data flagging was synchronized to the PINE-03 data acquisition interval.

At BRW, easterly winds and emissions from the Prudhoe Bay oil field can impact measurements (Kolesar et al., 2017; Creamean et al., 2018a). However, the oil field is located $\approx$

255   300 km east of Utqiaġvik. Because we cannot easily segregate Prudhoe Bay emissions from other local emissions, data coinciding with easterly winds are not flagged in this study. Although m_{BC} could be used as a proxy of potential oil field emissions only when the wind was from the clean sector (Sect. 3B and Fig. 3), it could also be due to recirculation of air masses containing emissions from the nearby community of Utqiaġvik.

260   **D. METEOROLOGICAL & AIR MASS DATA**

Local meteorology, including wind speed, wind direction, temperature, and relative humidity, were from BRW (see Data Availability). We used temperature data at 10 m AGL, which is nearest to the stack inlet height. To compare with INP data, which are collected at different timescales, meteorological datasets were also averaged over 6-hour time periods. Visibility and time-averaged

265   cumulative precipitation observations are not made at BRW, but are reported at the Wiley Post-Will Rogers Memorial Airport (ICAO: PABR) (71.285° N, 156.769° W) located ~ 7 km southwest of our field site.

270   **3. RESULTS AND DISCUSSION**

A. METEOROLOGY

Figure 1 displays meteorological data collected at BRW and their seasonality from October 19th, 2021, to December 31st, 2023. The overall

275   median temperature during our study period was −7.7 °C. There is a pronounced seasonality in temperature with a summer maximum of 19.7 °C
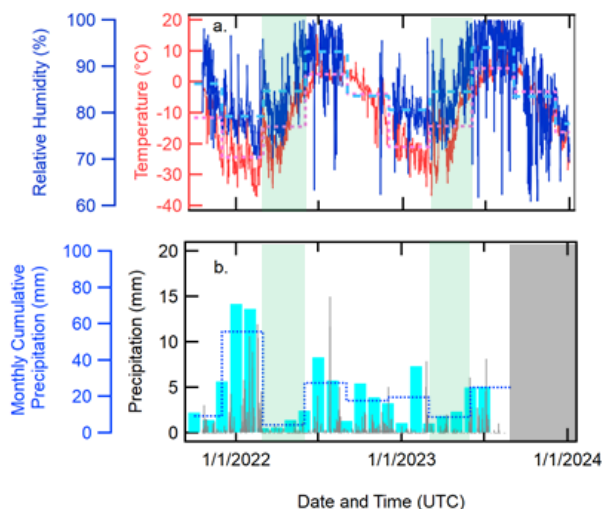
Figure 1. The time series of the 6-hour average temperature and relative humidity (a). Panel (b) displays the 6-hour average precipitation and monthly cumulative precipitation amounts. Dashed lines in each panel are mean seasonal values of individual measurements and the green shaded areas represent spring. Precipitation data from mid-August 2023 was not available, which is indicated by the grey shaded area. The relative humidity data from late August to early December 2022 is also missing.

and winter minimum of −37.2 °C. The median relative humidity (w.r.t. water) measured at BRW was 84.2 %. Particularly in winter, the air is typically near-saturation or supersaturation w.r.t. ice.

280   The seasonal average of measured visibility during our study ranged from 6.9 to 8.4 km without any distinct seasonal patterns. Both the lowest and highest average visibilities were measured in winter (low in 2022 and high in 2023). It is noteworthy that the 6-hour average visibility fluctuated throughout 2021 − 2023. The observed visibilities (not shown) are seasonally consistent but occasionally variable, implying a strong influence of localized events, such as

285   blowing dust, blowing snow, haze, fog, and sea spray (e.g., Chen et al., 2022; Quinn et al., 2007; DeMott et al., 2016).

Seasonal wind roses (6-hour time averaged) are plotted in Fig. 2. Median annual wind speed (± standard error) at BRW was 5.2 ± 1.6 m s^{-1}. During fall − winter, the seasonal average wind speed ranged from 6.4 m s^{-1} (SON) to 5.6 m s^{-1} (DJF). During spring − summer, the seasonal

290   average wind speed was similar (5.2 m s^{-1}). The maximum wind speed of 18.6 m s^{-1} was measured in November 2023. Although there was variability in wind direction measured at BRW, northeasterly winds prevailed as expected throughout the study period, which is predominantly from the clean air sector upwind of nearby settlements.
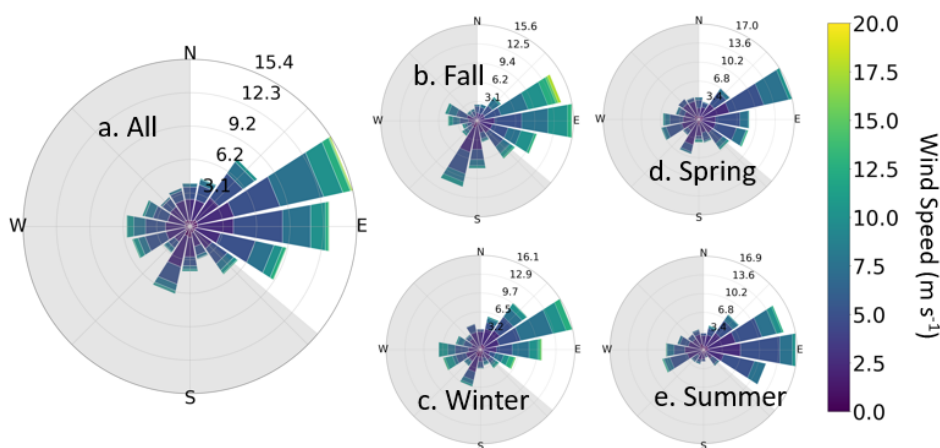
295   Figure 2. The wind speed and direction distributions during the ExINP-NSA (October 2021 − December 2023) are shown in the wind rose plot (a). The color scale of wind roses represents the wind speed observed at ground level (11 meters above sea level). Panels b − e show the wind roses for different seasons; fall (b), winter (c), spring (d), and summer (e). The grey shaded area represents the flagged wind direction (130° < WD < 360°) indicating potential contamination from the nearby community of Utqiaġvik.

300

The median value of monthly cumulative precipitation (± standard error) measured at the BRW site was 14.2 ± 4.1 mm. As seen in Fig. 1c, biannual maxima of measured precipitation in

winter (37.6 mm) and summer (26.4 mm) were found in 2021 – 2023; the lowest amount of precipitation occurred in spring (mean 6.6 mm).

B. AEROSOL ABUNDANCE

Figure 3 shows time series plots of n_{aer} and S_{aer}, black carbon mass, and submicron ion mass concentrations of arctic haze tracers. The total n_{aer} (cm^{-3}, shown with black dots) is plotted at 6 h averaged intervals. The overall median n_{aer} ($\pm$ standard error) during October 2021 − December 2023 was 156.3 ± 8.1 cm^{-3}, while the seasonal average n_{aer} was highest in summer (589.1 ± 54.2 cm^{-3}) and lowest in winter (227.2 ± 18.9 cm^{-3}). On average, spring also exhibited a relatively high n_{aer} of 431.4 ± 44.0 cm^{-3}, implying an influence of arctic haze (Quinn et al., 2007). Seasonal averages from this study are consistent with a long-term trend of monthly geometric means of condensation nuclei measured at BRW from 1977 to 1994 with an annual cycle of typical summer maxima and winter minima (Polissar et al., 1999).

Estimated m_{BC} values are also shown in Fig. 3a. With a median $\pm$ standard error value of 13.2 ± 3.4 ng m^{-3}, a strong winter maximum is apparent (up to 92.2 ± 3.9 ng m^{-3}) consistent with previous reports of seasonality of absorbing aerosol at BRW (e.g., Polissar et al., 1999; Delene and Ogren, 2002; Schmeisser et al., 2018). The highest m_{BC} was also observed during spring with ~ 40 ng m^{-3} on average. Previously, Barrett and Sheesley (2017) reported a peak elemental carbon (EC) mass concentration (m_{EC}) of ~ 100 ng m^{-3} measured at the ARM-NSA facility in February 2013. The authors identified fossil fuel combustion via transport as a
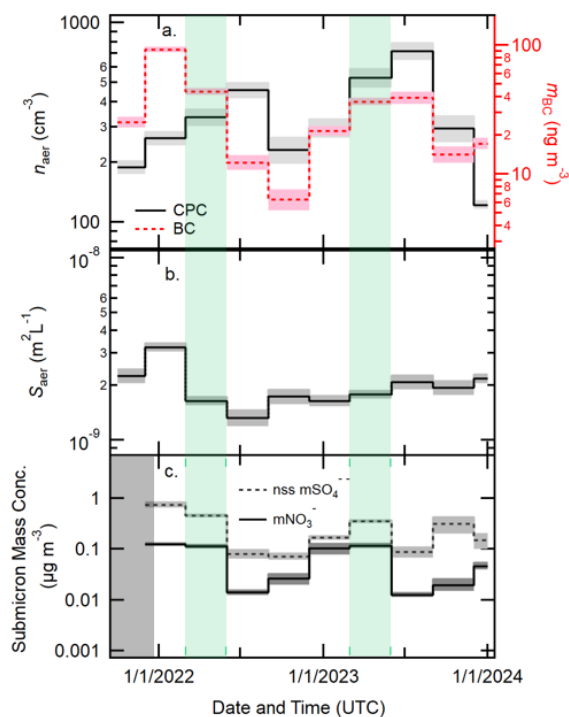
Figure 3. The seasonal average total particle concentration (n_{aer}, cm^{-3}, black line) and the mass concentration of black carbon (m_{BC}, ng m^{-3}, red line) (a). The time series of the seasonal average total surface area concentration (S_{aer}, m^2 L^{-1}) (b). Submicron NO$_3^-$ and nss SO$_4^=$ ion mass concentrations (c). The shaded area in (a) and (b) represent standard errors of each measurement. The uncertainties in (c) are reported in the chemical data. The grey shaded area shows the data missing period, and the green shaded area represent the Arctic spring during our study periods.

significant source of ambient organic carbons, accounting for > 60% of mass, during their year-round study period from the summer of 2012. Moffett et al (2022) measured low m_{EC} near Utqiaġvik during summer, suggesting biomass burning and wildfire contribution as a minor source of EC.

The median S_{aer} (± standard error) at BRW was $1.2 \times 10^{-9} \pm 8.4 \times 10^{-11}\,\mathrm{m^2\,L^{-1}}$. Seasonal variability in S_{aer} is shown in Fig. 3b, with seasonal average maxima and minima found in winter 2021 (DJF; $3.2 \times 10^{-9} \pm 1.8 \times 10^{-10}\,\mathrm{m^2\,L^{-1}}$) and summer 2022 (JJA; $1.3 \times 10^{-9} \pm 1.3 \times 10^{-10}\,\mathrm{m^2\,L^{-1}}$), respectively. The estimated median single particle surface area (i.e., S_{aer}/n_{aer}) from BRW ($< 0.02\,\mathrm{\mu m^2}$) is substantially smaller than at ARM'sSouthern Great Plains (SGP; $1.4\,\mathrm{\mu m^2}$) and Eastern North Atlantic (ENA; $0.05\,\mathrm{\mu m^2}$) observatories, as derived from Wilbourn et al. (2024), suggesting a predominance of small particles at BRW. We note that S_{aer} is derived by means of nephelometer measurements at both BRW and -ENA. *In-situ* coarse aerosol size distribution measuring instruments, such as an optical particle counter and an aerosol particle sizer, were not operational during any of our campaigns.

The min-max ranges of nss $SO_4^=$ and NO_3^- at BRW are $0.003 - 2.2$ and $0.005 - 1.2\,\mathrm{\mu g\,m^{-3}}$, respectively, during our field study. Clear seasonal cycles were found for arctic haze tracers, including nss $SO_4^=$ and NO_3^- (Fig. 3c). With a median mass concentration of $0.2 \pm 0.02\,\mathrm{\mu g\,m^{-3}}$, the maximum mass concentration of nss $SO_4^=$ was found in spring on average ($0.4 \pm 0.03\,\mathrm{\mu g\,m^{-3}}$). Likewise, NO_3^- also had the highest seasonal average of $0.1 \pm 0.01\,\mathrm{\mu g\,m^{-3}}$ in spring. The observed spring maxima and seasonality in particulate nss sulfate and nitrate mass concentrations can primarily be attributed to the long-range transport of arctic haze (Quinn et al., 2007). We also note that, because these aerosol composition values are for submicron soluble aerosol, these chemistry measurements may not directly relate to INPs, as INPs preferentially involve insoluble supermicron particles (e.g., Mason et al., 2016).

360

365

370

Figure 4. INP concentrations ($n_{\mathrm{INP}}(T)$) measured at BRW. The 'all' dataset collected throughout the campaign is shown in (a). The segregated datasets collected during the 'clean' periods (clean data) and 'contaminated' periods (presumably contaminated data) are shown in (b) and (c). Each point represents a 6-hour time-averaged concentration. The color scale indicates the measured freezing temperature. Individual data points are temperature binned for 1 °C. The campaign mean and median n_{INP}(-25°C) are shown with dark blue and cyan lines.
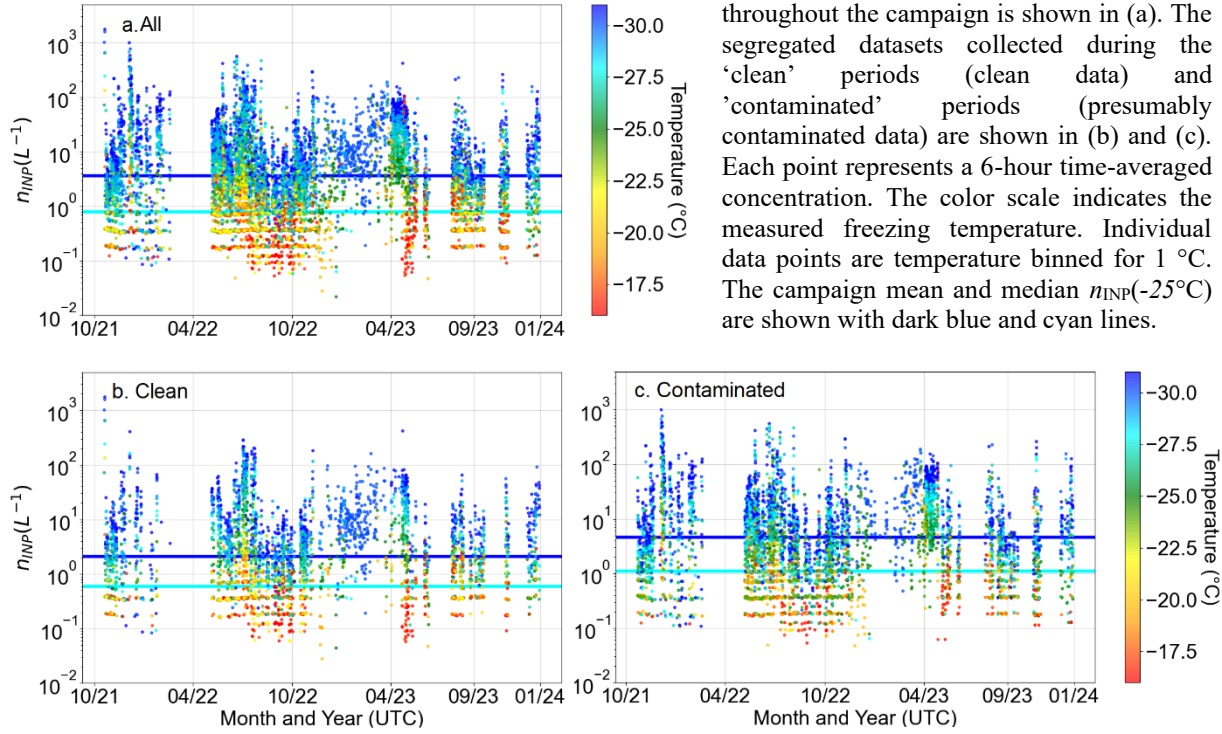
C. Ice-Nucleating Particle Abundance

Shown in Fig. 4 is the comparison of online $n_{\mathrm{INP}}(T)$ based on (a) the 'all' dataset (i.e., all valid

380   measurements retained); (b) 'clean' data subset as determined following the standard BRW wind protocols and removing flagged PINE-03 data for operational issues; and (c) 'contaminated' subset following the wind and PINE-03 data screening protocols. The time series of 6 h averaged $n_{\mathrm{INP}}(T)$ from BRW with a temperature resolution of 1 °C is shown in each panel, with different colors scaling to freezing temperature between −16 °C (red) and −31 °C (blue). For the 'all' dataset,

385     $n_{\mathrm{INP}}(T)$ data are displayed with a total of 14,318 data points of 6 h averaged $n_{\mathrm{INP}}(T)$ collected during our study period. Data gaps in spring 2022, summer 2023, and fall 2023 seen in Fig. 4a are due to maintenance.

    As shown in Fig. 4, $n_{\mathrm{INP}}(−25°C)$ values ± standard errors are $3.6 \pm 1.2\,\mathrm{L^{-1}}$, $2.1 \pm 0.6\,\mathrm{L^{-1}}$, and $4.6 \pm 1.5\,\mathrm{L^{-1}}$ for all, clean, and contaminated datasets, respectively. Likewise, the medians of

390     $n_{\mathrm{INP}}(−25°C)$ are similarly sorted with $0.8 \pm 0.4\,\mathrm{L^{-1}}$, $0.6 \pm 0.2\,\mathrm{L^{-1}}$, and $1.1 \pm 0.5\,\mathrm{L^{-1}}$ for all, clean, and contaminated datasets. As anticipated, the contaminated dataset exhibited a higher mean than others, likely reflecting the influence of emissions from Utqiaġvik. The distribution of $n_{\mathrm{INP}}(T)$ is

skewed due to the occurrence of positive extremes. Thus, we report the median in addition to the mode.

395 **D. FREEZING EFFICIENCIES**

Figure 5 shows the 6-hour average $n_{INP}(T)$, *IAF* (i.e., $n_{INP}(T)/n_{aer}$), and $n_s(T)$ (i.e., $n_{INP}(T)/S_{aer}$) at selected temperatures (−20, −25, and −30 °C). A noticeable difference between $n_{INP,all}$ and $n_{INP,clean}$ is seen in Fig. 5. Typically, we observe that $n_{INP,all}$ exceeds $n_{INP,clean}$ as the all/clean ratio is typically > 1 (Fig. 5g − i). In winter, the ratio is especially high. During this time, southwesterlies,

400 presumably contaminated by recirculated emissions from the town, contain abundant INPs. In winter 2021, the seasonal m_{BC} of 92.2 ng m^{-3} is higher than the overall average m_{BC}, which indicates the impact of Utqiaġvik emissions (e.g., fuel burning). We note that a seasonal average m_{BC} of 21.5 ng m^{-3} in winter 2022 is lower than the overall average m_{BC}, suggesting that local emissions may not have made a prominent contribution to m_{BC} observed at BRW in winter 2022

405 and that BC is in part from long-range transport as suggested by previous studies (Barrett and Sheesley, 2017; Moffett et al., 2022). High INP abundance and freezing efficiencies not associated with local emissions were observed in spring 2023. This coincided with a large temporal change in ambient temperature and minimal seasonal precipitation (Fig. 1), as well as observed high concentrations of arctic haze tracers (Fig. 3). Hence, this high INP episode may have been triggered

410 by a combination of factors. Average *IAF*s at −20, −25, and −30 °C are similar between the all and clean datasets (1.7 x 10^{-6} − 1.1 x 10^{-4}). Conversely, $n_s(T)$ exhibits a slight deviation between the two datasets with 'clean' having a lower average $n_s(T)$ of ≈ 3.2 × 10^8 m^{-2} to ≈ 1.1 × 10^{10} m^{-2} than the 'all' dataset (≈ 9.4 × 10^8 m^{-2} to ≈ 1.6 × 10^{10} m^{-2}). In order to relate our results to BRW baseline aerosol measurements and previous literature, 'clean' sector data are used for further analysis in

415 this study.
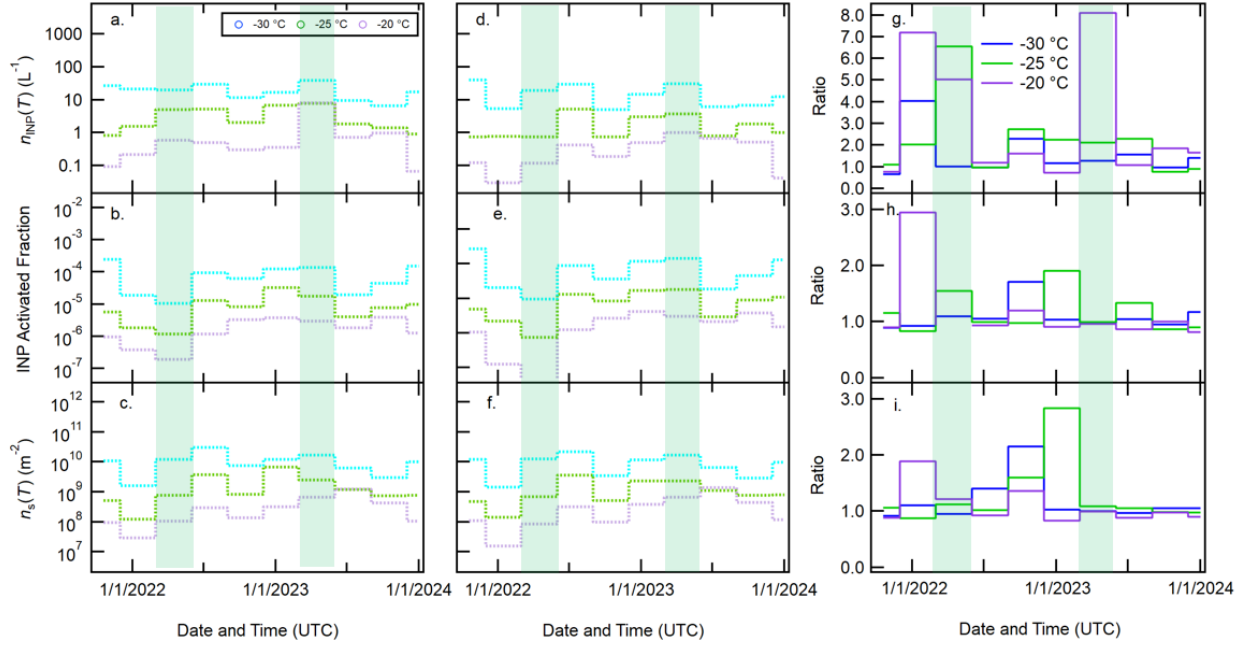
Figure 5. The seasonallyaveraged $n_{INP}(T)$, IAF, and $n_s(T)$ at selected temperatures for the 'all' dataset (a – c) and screened 'clean' data subset (d – f) at BRW. Panels (g – i) show the ratio of all/clean data seasonally. The lines represent seasonal average values for the measured periods. Green shaded areas represent the arctic spring periods.

A series of histograms displaying probability densities and relative frequency of 6-hour averaged $n_{INP}(T)$ and $n_s(T)$ data from PINE-03 are shown in Fig. 6 with a temperature resolution of 1 °C for BRW. The mode $n_{INP}(T)$ and $n_s(T)$ are reasonably comparable to our average $n_s(T)$ for data with the given bin-resolved data density ($n > 224$) despite some inclusion of outliers at low $n_{INP}(T)$ and $n_s(T)$. For the $n_s(T)$ distributions, fitted $n_s(T)$ values from this study are also superimposed on each histogram to show reasonable agreement with the average values of the log-normal $n_s(T)$ distribution. Seasonal breakdowns of the $n_{INP}(T)$ and $n_s(T)$ histograms are shown in SI. Figs. S2 and S3 (SI. Sect. 4).
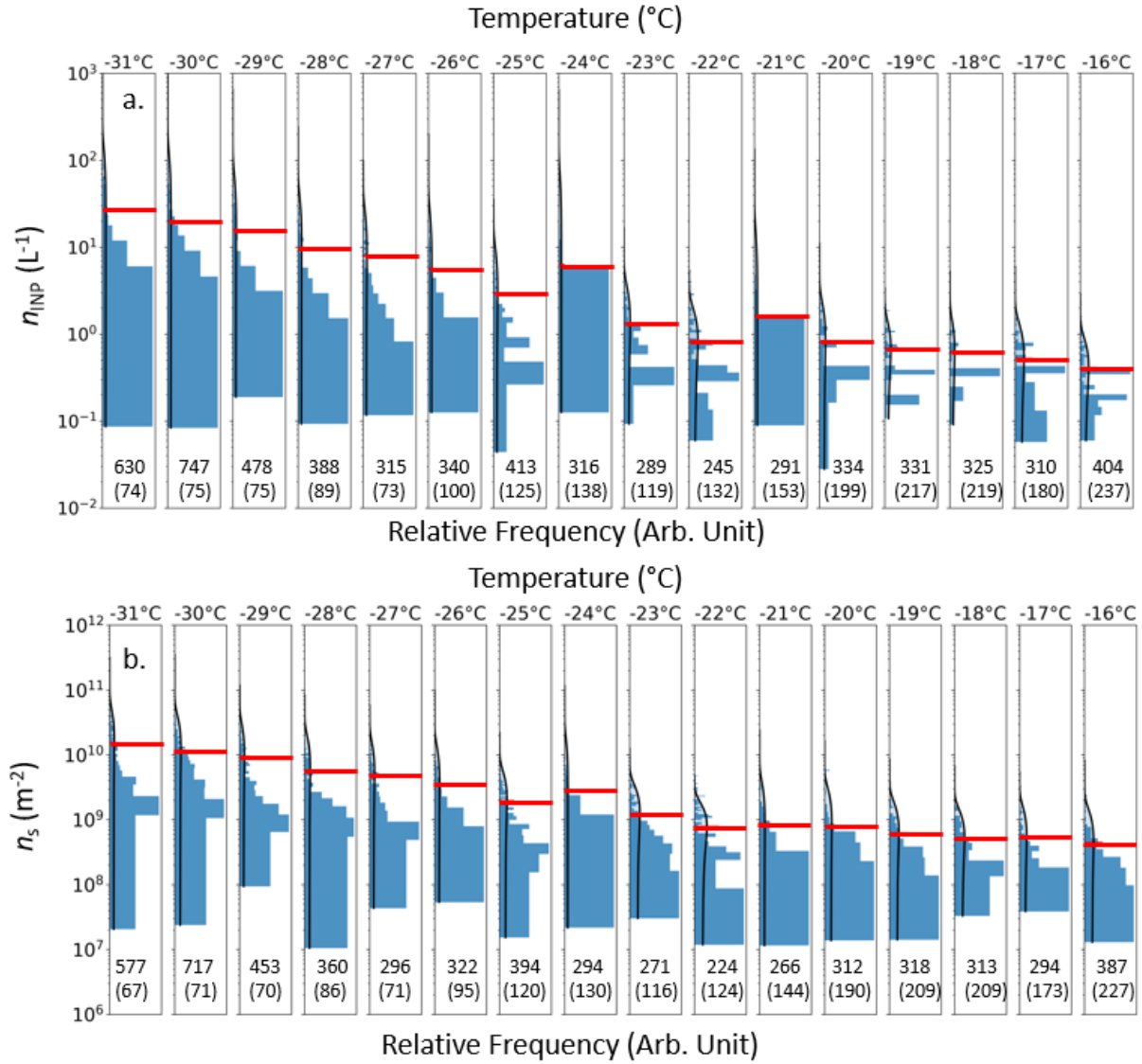
Figure 6. Histograms of the PINE-03-based $n_{INP}(T)$ and $n_s(T)$ Gaussian distribution with one degree temperature binning are shown in (a) and (b). The 'clean' data were used to generate this figure. The data covers a statistically validated freezing temperature range (−16 to −31 °C) for October 2021 − December 2023. Individual data densities are shown at the bottom of each column, and zero INP number counts, included in time-averaged n_{INP} calculation, are shown in parentheses. Relative frequencies (Arbitrary Unit) for each degree are shown at the bottom of each sub-panel. Red horizontal lines in each relative frequency distribution sub-panel represent the average. The Gaussian log-normal fit is shown for each degree of binned data (black lines).

Figure 7 shows 6-hour averaged PINE-03-measured n_{INP} and n_s data from BRW as a function of freezing temperatures (1 °C resolution) as box plots (a − b). Clean data were used to generate Fig. 7 while Fig. S4 is based on 'all' data for comparison (SI Sect. S5). Also shown in Fig. 7a are previously reported $n_{INP}(T)$ data collected from or near the North Slope of Alaska (see Sect. 1D and references therein). The data collected in this study are generally comparable to data

presented in Barr et al. (2023; B23), Inoue et al. (2021; I21), Sanchez-Marroquin et al. (2023; S-M23), and Prenni et al. (2007; P07) as their data overlap with our $25^{th} - 75^{th}$ percentile $n_{INP}(T)$ data in one temperature bin at least. On the other hand, the $n_{INP}(T)$ range for some studies is much lower than the $n_{INP}(T)$ range of ExINP-NSA, potentially due to differences in INP sources that those studies investigated (e.g., sea spray aerosols without sea ice coverage). Figure 7b shows the $n_s(T)$ data, as well as associated exponential fits. Following Li et al. (2022) and Wilbourn et al. (2024), we computed $n_s(T)$ parameterizations that fit the average values of the log-normal $n_s(T)$ distribution as a function of freezing temperatures as follows:

$$n_s^{avg}(T) = exp\left(24.250 \times exp\left(-exp(0.060 \times (T + 9.700))\right) + 4.995\right) \qquad r = 0.99$$

$$-31\,°C \leq T \leq -21\,°C. \qquad\qquad [2]$$
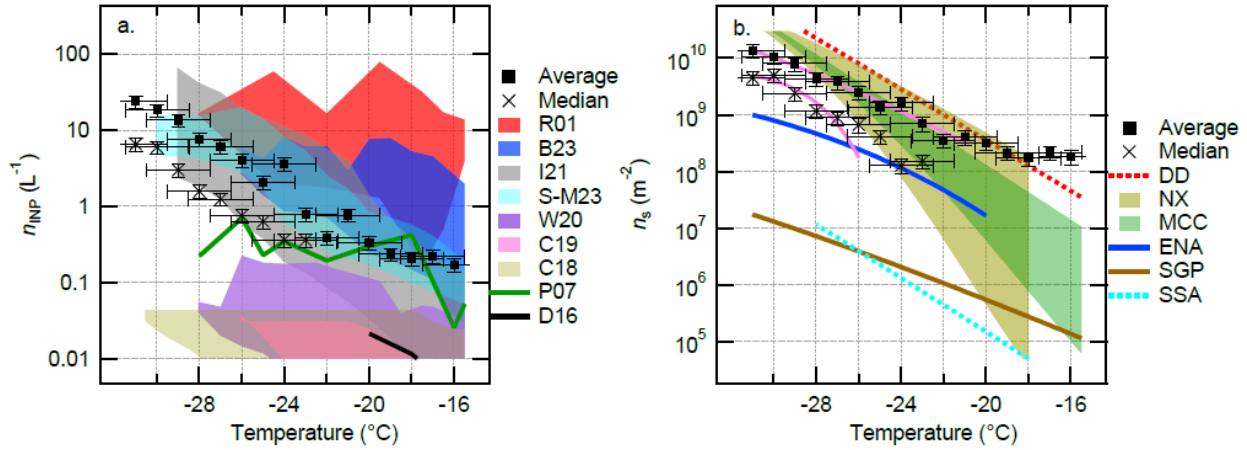
Figure 7. Box plots of the PINE-03 based $n_{INP}(T)$ (a) and $n_s(T)$ (b) data from BRW in 1 degree temperature bins for a statistically validated freezing temperature range (−16 to −31 °C). The 'clean' data were used to generate this figure. Boxes represent average (black solid symbol) and median (black cross symbol) statistics. The color-shaded area in (a) shows the maximum and minimum $n_{INP}(T)$ measured by previous INP studies at or in the proximity of BRW (see Table A1 and Sect. 1 for references). The reference $n_s(T)$ data in (b) are adopted from W24 (Wilbourn et al., 2024 and references therein) for SGP, ENA, desert dust, sea spray aerosol, illite NX, and microcrystalline cellulose. Pink lines are fits to BRW data from this study. The uncertainties in $n_{INP}(T)$ and $n_s(T)$ are also adopted from W24.

The parameterization offered in this study is limited to ≤ −21 °C. Below −21 °C, a constant increase in $n_s(T)$ towards low freezing temperature is seen, whereas a plateau of high $n_s(T)$ is found between −21 °C and −16 °C, at which our INP data are validated within errors discussed in SI Sect. S2. However, we cautiously note that the flattening of the concentrations warmer than −21 °C is a spurious result mainly due to the instrument resolution. As described in Sect. 2B, the minimum resolvable INP value is 0.02 L^{-1} on a 6-hour time average, but the non-time-averaged minimum n_{INP} detection limit is in fact ~ 0.2 L^{-1}. This floor approximately intersects a plateau

region where the data remains remarkably steady near −20 °C (i.e., close to the beginning of the flattening). We would expect a loss of sensitivity to result in an undercounting of values as mostly 0s are averaged into data. Nevertheless, it appears likely that the flattening is a consequence of the resolution floor of the system and its operational configuration at BRW.

The comparison between $n_s(T)$ data from this study and reference spectra shown in Fig. 7b reveals that ice nucleation efficiencies of aerosols collected at ground level at BRW are equivalent to, or higher than, desert dust studied in Ullrich et al. (2017) above −20 °C. This outcome was expected as the aerosol population at BRW is presumably not purely composed of desert dust. Indeed, many previous studies suggest the potential influence of highly active biogenic INP in the region (Inoue et al., 2021; Creamean et al., 2022). While a partial overlap of our $n_s(T)$ with illite NX (mineral dust proxy) and microcrystalline cellulose (MCC; non-proteinaceous organic surrogate) spectra are seen in a few temperature bins in the middle range (i.e., −27 °C < T < −19 °C), reference spectra of these compositions cannot solely explain the overall $n_s(T)$ trend from BRW. The sea spray aerosol (SSA) $n_s(T)$ parameterization spectrum from McCluskey et al. (2018) shows a less active trend and is not comparable to the BRW data, implying aerosols collected at BRW are different from SSAs seen in McCluskey et al. (2018) and perhaps predominantly composed of nss and non-SSA compounds. The link between these chemical compounds to INP is not straightforward. Without detailed size-dependent composition and ice residual chemistry data, further discussion cannot be made in this study. It is also worth noting that a substantial portion of the PINE measurement period was during winter when the adjacent ocean was capped by sea ice. Figure 8 below and Fig. S5 (SI Sect. 6) show seasonal n_s parameterizations.
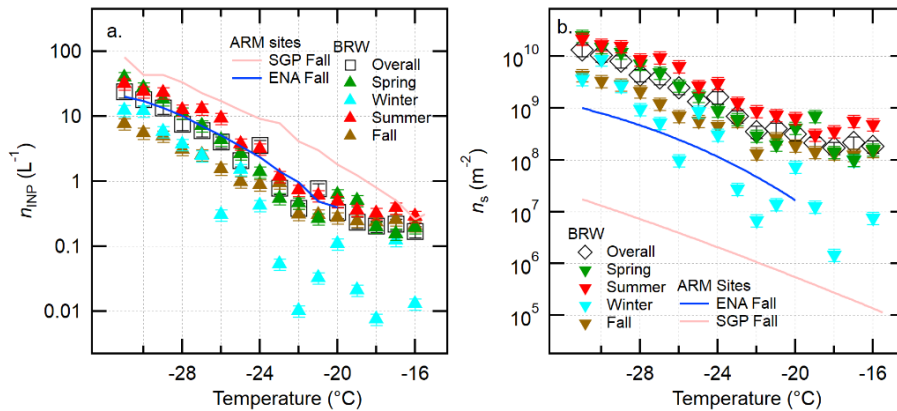
Figure 8. Seasonal breakdowns of the PINE-03 based $n_{INP}(T)$ and $n_s(T)$ data are shown in (a) and (b), respectively. The uncertainties in $n_{INP}(T)$ and $n_s(T)$ are also adopted from W24.

Shown in Fig. 8 is seasonality of 6-hour averaged PINE-03-measured $n_{INP}(T)$ and $n_s(T)$ data from BRW. When comparing seasonally-averaged $n_{INP}(T)$ values (Fig. 8a), it is notable that

$n_{INP}(T)$ in spring and summer at BRW is consistently higher than $n_{INP}(T)$ from other seasons. The observed difference in $n_{INP}(T)$ can be in part attributed to arctic haze episodes that occur during arctic spring (Rogers et al., 2001; Quinn et al., 2007) and local sediment exposure to air after springtime melt (Cox et al., 2019; de Boer et al., 2019) while further quantitative analysis with high-time-resolution data is necessary. Fall $n_{INP}(T)$ data from BRW in comparison to $n_{INP}(T)$ spectra from mid-latitude sites (i.e., SGP and ENA) in the same season suggest that INP abundance is lowest in the Arctic (at least for fall). The maritime $n_{INP}(T)$ represented by the ENA measurements is consistently higher than fall data from BRW and lies toward the upper bound of the overall BRW data. We note that the relative abundance of aerosols at ENA is on average more than twice as high as observed at BRW for our study period. Continental INPs from SGP exceed BRW $n_{INP}(T)$ below -20 °C. It is worth noting that the high variability in BRW winter data is partially due to the high frequency of zero INP counts collected in this season ($\approx 66\%$) as compared to other seasons ($\approx 21 - 23\%$; Fig. 6). PINE-03 is designed to utilize ambient moisture to saturate the chamber during expansion cooling and for maintaining chamber dew point temperature above freezing. Dry winter conditions often lowered dew point and hindered INP measurements. Regardless, patterns in $n_{INP}(T)$ and $n_s(T)$ can still be compared as representative of each season because our temperature-binned $n_{INP}(T)$ and $n_s(T)$ data offer at least 22 and 21 data points in each bin (see SI Figs. 2 and 3).

Seasonal variability in $n_s(T)$ is obvious in Fig. 8b. In general, two data subsets (i.e., higher $n_s(T)$ in spring and summer and lower $n_s(T)$ in fall and winter than the overall data) define the $n_s(T)$ characteristics from this study at low temperatures. Surprisingly, BRW $n_s(T)$ exceeds SGP and ENA $n_s(T)$ values by at least one order of magnitude across the freezing temperatures analyzed in this study, suggesting there are unique INP properties in the region.

Correlations between detectable n_{INP} at selected temperatures (i.e., -20, -25, and -30 °C) vs. measured variables averaged for 6 hours suggest the following: (1) S_{aer} and m_{BC} are well correlated ($r = 0.7$, $p < 0.05$), indicating some BC was externally mixed and available on aerosol surfaces at BRW during the study period and, (2) at a freezing temperature of -25 °C, there is a positive correlation between n_{INP} and precipitation amount ($r = 0.7$, $p < 0.05$; $N = 68$), which could suggest a contribution of hydrometeors to n_{INP}, potentially derived locally in part by blowing snow (Chen et al., 2022). However, the correlation between precipitation amount and INP abundance for other temperatures is weak ($|r| \lesssim 0.2$, $p < 0.05$). Therefore, the direct relationship between INP

and precipitation at BRW is not conclusive. It is noteworthy that our previous study with PINE-03 from a mid-latitude continental setting showed n_{INP} values decreased immediately after precipitation events while IAF and n_s remained consistent (Wilbourn et al., 2024).

While 6-hour time-averaged data is unavailable from the ion chromatography filter measurements (Sect. 2C.4), seasonal means of nss $SO_4^=$ correlate well with NO_3^- ($r = 0.7$), wind direction ($r = 0.7$), S_{aer} ($r = 0.7$), and m_{BC} ($r = 0.9$). These correlations imply that arctic haze coincidentally delivers nss $SO_4^=$, BC, and NO_3^- with large particle surface areas. On the other hand, nss $SO_4^=$ shows a reciprocal relation with temperature ($r = -0.7$), attributed to the winter − spring dominance of arctic haze. Furthermore, seasonal mean nss $SO_4^=$ weakly correlates with seasonal precipitation amount ($r = 0.5$). This implies that wet deposition during arctic haze may contribute to observed high nss $SO_4^=$ via evaporation and/or sublimation of the precipitation near the surface.

E. AIR MASS TRAJECTORIES AND PARTICLE ABUNDANCE

The n_{INP} observations are positively correlated with a regional climate index ($r \approx 0.4$ at $-31\ °C$) that encodes the juxtaposition of the Aleutian Low and the Beaufort High (Cox et al., 2019). This indicates that higher INP concentrations tend to be associated with air advecting northward through the Bering Strait before dispersing eastward over the NSA during periods when the dominant easterlies of the Beaufort High are weak or reversed. In this section, we further analyze the source regions using back trajectories.

Table 2 lists periods of high- and low-INP episodes and associated $n_s(T)$ parameters found at BRW. Since $n_s(T)$ accounts for both INP and aggregate aerosol properties, we use it as a representative ice nucleation efficiency index to select high- or low-INP periods in this study. High INP episodes are defined by n_s values exceeding their 75th percentile values at -20, -25, and $-30\ °C$. In contrast, low INP episodes correspond to n_s at the three temperatures below the 25th percentile.

Table 2. List of high- and low-INP periods from BRW. *Clean data (A fully extended table is available in supplemental materials; SI Table3)

Data	ID	Date & Time (UTC)	n_s(m^{-2})		
			−30 °C	−25 °C	−20 °C
	1	5/9/2022 0:00	2.1E+10	2.2E+09	5.7E+08
High	2	5/31/2022 18:00	2.4E+10	2.8E+09	7.2E+08
INP	3	6/20/2022 6:00	1.6E+10	2.7E+09	3.3E+08
n = 15	4	6/20/2022 0:00	4.0E+10	6.9E+09	3.3E+08
	5	6/16/2022 6:00	3.9E+10	7.6E+09	1.3E+09
	6	6/25/2022 0:00	5.9E+10	8.9E+09	5.9E+08
	7	*6/24/2022 12:00	1.7E+10	2.6E+09	5.3E+08
	8	7/3/2022 18:00	1.0E+11	1.7E+10	3.5E+09
	9	7/3/2022 12:00	6.0E+10	7.3E+09	3.7E+08
	10	7/2/2022 18:00	8.6E+10	1.1E+10	8.4E+08
	11	7/2/2022 6:00	1.9E+10	6.7E+09	8.2E+08
	12	4/2/2023 18:00	2.4E+10	3.9E+09	5.6E+08
	13	4/22/2023 0:00	2.5E+10	1.7E+09	4.7E+08
	14	4/30/2023 12:00	2.2E+10	4.5E+09	3.3E+08
	15	6/3/2023 18:00	4.2E+10	2.8E+09	1.6E+10
	1	11/22/2021 0:00	7.7E+08	0	0
Low	2	11/21/2021 12:00	4.0E+08	0	0
INP	3	11/21/2021 6:00	1.4E+09	0	0
n = 15	4	11/29/2021 6:00	0	0	0
	5	11/28/2021 18:00	0	0	0
	6	12/29/2021 6:00	0	0	0
	7	*1/03/2022 18:00	0	0	0
	8	*1/08/2022 18:00	0	0	0
	9	1/14/2022 18:00	4.3E+08	0	0
	10	1/14/2022 12:00	9.9E+08	0	0
	11	1/13/2022 18:00	0	0	0
	12	*1/21/2022 06:00	0	0	0
	13	*2/02/2022 00:00	0	0	0
	14	*2/06/2022 12:00	0	0	0
	15	2/10/2022 12:00	0	0	0

560

Back trajectories are plotted in Figure 9 (for seasonal subsets, see SI Sect. S7). For our study period, 15 of 3176 trajectories are considered high INP cases and displayed in Fig. 9b. Some air masses during the high INP period show a westward trajectory from northeastern Alaska. While they appear to pass over the Prudhoe Bay oil field region, distinguishing the influence from that

565 region would require further analysis and attention to resolution beyond the scope here. Besides Prudhoe Bay, maritime contributions originating from the North Pacific Ocean are a significant source of high INP trajectories at BRW especially in the summertime (SI Figs. S6 and S7).
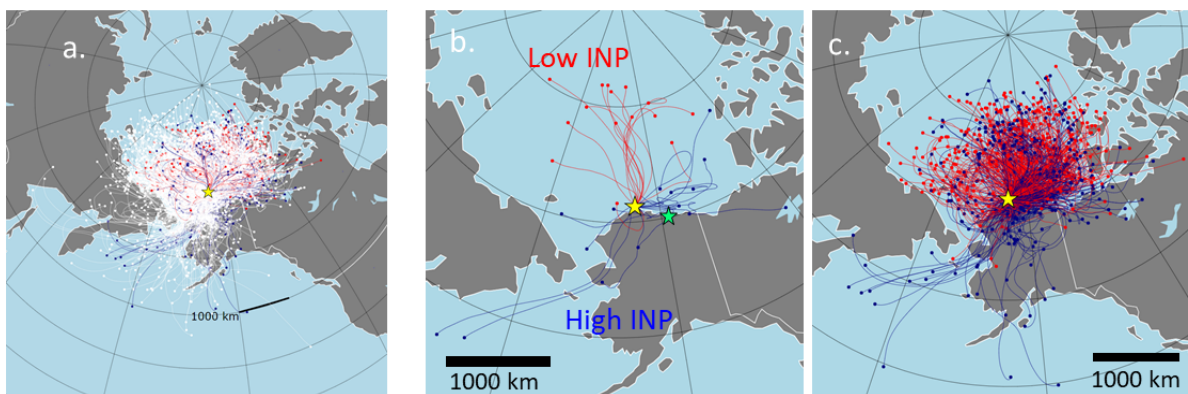
Figure 9. Air mass origins and back trajectories from the inlet height for BRW (yellow star). The Prudhoe Bay location is indicated by the green star in panel (b). All trajectories for the time period October 2021 − December 2023 are shown in (a). The air mass trajectories during high- and low-INP episodes are shown in blue and red colors. Panel (b) represents the data selected with a low − high threshold of the 25th − 75th percentile based on $n_s(T)$, at all −30, −25, and −20 °C. Panel (c) represents the data selected with a low − high threshold of the 25th − 75th percentile based on $n_s(T)$ at any −30, −25, and −20 °C. The details of high- and low-INP episodes in separate panels are shown in SI Figs. S6 and S7. The seasonal breakdowns of the *trajectory data* are shown in SI Figs. S8 and S9.

The high- and low-INP episodes for the any Ts case based on 72-hour air mass back trajectories, as displayed in Figure 9c, suggest air mass contributions from North America (particularly the southern Alaska region) and Russian/Siberian Coast are associated with high INP concentrations. A total of 291 and 364 trajectories (out of 3,176) correspond to high- and low-INP events, respectively (Tables 2 and 3). These patterns could suggest that terrestrial sources, potentially influenced by transported biomass burning material in spring and summer, are contributing to the elevated INP levels in BRW. While the exact sources of INPs from high latitudes remain uncertain, previous studies point to biogenic aerosols as a possible source in the Arctic (Inoue et al., 2021; Creamean et al., 2022; Sanchez-Marroquin et al., 2023). In comparison, Moffett et al. (2022) identified the influence of transported biomass burning materials from Russia/Siberia as a key contributor to arctic INP levels, while Irish et al. (2019) reported the presence of INPs in the sea surface microlayer. Similar high INP episodes have been observed in other arctic and sub-arctic regions. For instance, a study in Iceland reported INP concentrations of over 100 L^{-1} at −26°C (Sanchez-Marroquin et al., 2020), and Southern Alaska showed around 6 L^{-1} (Barr et al., 2023), reinforcing the importance of dust and other terrestrial sources in these regions.

As seen in Fig. 9c, at BRW low INP episodes coincide with air masses originating from coastal regions of the North American Arctic and contributions from the high Arctic account for > 60 % as compared to other source regions. As discussed in several previous studies (Creamean

595   et al., 2018b; Creamean et al., 2019; DeMott et al., 2016), maritime SSAs are less active as INPs relative to terrestrial dust particles.

To contextualize the source of INPs in northern Alaska and the reason for $10 - 1000$ times greater efficiency in arctic INPs, local and synoptic meteorological influences on INPs must be investigated. In particular, the role of local blowing snow, resuspension of surface materials, and

600   synoptic air mass transport from the warm Pacific Ocean on INPs for selected high- and low-INP episodes can be investigated. Assessing relationships between a regional climate index, known large-scale meteorological patterns influencing northern Alaska, and INP properties will provide an insight on arctic INP properties. Further efforts to correlate INP properties in fall during identified high INP periods with other aerosol and atmospheric parameters will shed additional

605   light on arctic INPs. Such an analysis will be important to comprehensively understand mechanisms and projections of arctic warming beyond the sea ice albedo effect.

4. CONCLUSION

Continuous n_{INP} data were measured in the Alaskan Arctic from October 2021 through December 2023. We find a factor of $10 - 1000$ times greater efficiency in the arctic INPs through

610   heterogeneous freezing at sea level during autumn compared to those found previously (Wilbourn et al., 2024) at the mid-latitude ARM sites using the same instrumentation. Specifically, we find relatively low concentrations of aerosol surface area (Fig. 3b) and contrasting high INP concentrations (Fig. 4) at BRW relative to previous observations atARM's SGP and ENA sites. In each of these studies, the same PINE-03 system was deployed for an extended time period. Thus,

615   while the PINE-03 has limitations (for example insensitivity to INPs with freezing temperatures > -16 °C), the relative comparisons among these locations are instructive.

Our analysis of this multi-season INP dataset from BRW offered insight on the variability of INP abundance and revealed seasonality in INP properties. Spring showed profound INP abundance and freezing efficiencies, presumably due to arctic haze events. As previously shown,

620   some arctic haze tracers, such as particulate nss sulfate and nitrate, were found to be higher in spring in our study period than in other seasons. From back trajectory analysis, it is found that air masses connected to high INP episodes can come from all directions while low INP episodes are strictly from north. More specifically, air masses observed during high INP episodes in spring tended to come from terrestrial regions (Central Alaska).

625   Our n_{INP} data show very high freezing efficiency of INPs across the measured temperatures as compared to the previous mid-latitude INP measurements made by the same instrument, as well as observed high n_{INP} above −21 °C throughout the year. This data suggests the persistent presence of high temperature INPs in Arctic Alaska. Distinct different freezing efficiencies of aerosols observed for the arctic site as compared to the mid-latitude sites indicate the necessity of

630   considering emission source regions yet not to merge whole regions into one because INP data is region dependent.

Long-term INP datasets, such as that presented here, are lacking in the arctic region but are needed to improve representation of clouds in numerical models. To this end, we developed a parameterization for ice nucleation active surface site density covering −31 to −21 °C. For

635   temperatures higher than −21 °C, INP concentrations were sufficiently low to approach the boundaries of what is detectable given the experimental design, a factor that should be considered for future studies (e.g., examining larger air volume or recreating particle-laden conditions by virtual air mass concentration). This dataset also complements shorter INP datasets previously made in the same region. It will be useful to improve atmospheric models to simulate cloud

640   feedback and determine their impact on the global radiative energy budget. Whether this parameterization can only be applied to ground-level INPs or if vertical INP gradients might affect their utility in modeling cloud processes should be verified. Together with the INP data, additional aerosol data, such as coarse mode size distributions, particle chemical composition and mixing state (deployed at BRW in October 2024), as well as vertical INP profiles, would allow us to

645   further understand the implications of this dataset for clouds, precipitation, and regional weather, as well as overall ambient ice nucleation abundance in the NSA region.

APPENDIX A PREVIOUS STUDIES

Arctic INPs have been reported from the NSA region in several previous studies. The present study reports the first n_{INP} data measured at the BRW site. A summary of 7 studies that report n_{INP} from or near the NSA is provided in Table A1.

Table A1. A summary of past INP abundance measurements that took place near the BRW monitoring site.

Study	Measured freezing Ts (°C)	n_{INP} (L^{-1})	Period	Region	Instrument	Platform
Present Study	−16 to −31	*0.4 to 8.3 **0.6 to 27.0	Oct. 2021 to December 2023	NSA	PINE-03	Ground-Site (BRW)
Prenni et al., 2007 (P07)	≈ −8 to −28	0.16 (mean)	Oct. 2004	NSA	Online CFDC	University of North Dakota's Citation II aircraft
Fountain and Ohtake, 1985 (F&O85)	−20	0.17 (mean)	Aug. 1978 to Apr. 1979	NSA	Offline diffusion chamber	Ground-Site (Not specified)
Creamean et al., 2018a (C18)	≈ −5 to −30.5	≈ 2.6 x 10^{-5} to 4.4 x 10^{-2}	Mar. to May 2017	Oliktok Point, NSA	Offline droplet freezing assay	Ground-Site (ARM AMF-3)
DeMott et al., 2016 (D16)	≈ −12 to −20	≈ 2.0 x 10^{-4} to 2.0 x 10^{-2}	Summer 2012	Central Bering Sea	Online CFDC	Research Vessel Araon
Sanchez-Marroquin et al., 2023 (S-M23)	≈ −14 to −30	≲ 40	Mar. 2018	NSA coast to Yukon, Canada	Offline droplet freezing assay	UK's BAe-146 FAAM Aircraft
Rogers et al., 2001 (R01)	−10 to −30	≲ 57	May 1998	Offshore NSA	Online CFDC	NCAR C-130 Aircraft
Inoue et al., 2021 (I21)	≈ −7.5 to −29.5	≈ 5.0 x 10^{-4} to 10^{2}	Nov. 10–21, 2018	Chukchi Sea NSA	Offline droplet freezing assay	Research Vessel Mirai

*clean median; **clean average; the data screening protocol is described in Sect. 2E.

APPENDIX B BACKTRAJECTORY ANALYSIS

Trajectories were based on the Global Data Assimilation System (GDAS) and calculated using the Hybrid Single-Particle Lagrangian Integrated Trajectory (HYSPLIT) model (Rolph et al., 2017; Stein et al., 2015) to compute archive trajectories every 6 hours during the sampling period. Each 72-hour backward trajectory was calculated at the sampling inlet height (~ 12 m AGL). Our analysis protocols follow those of Wilbourn et al. (2024). Back trajectory origins were classified into broad regional categories, including the major oceans and continents, as described in SI Sect. 12 of Wilbourn et al. (2024).

Source points are assigned to the final back trajectory locations at 72-hr. Besides land and ocean, we also determine if the source was over an area covered in sea ice. The sum of rainfall is calculated at each height, and if the rainfall amount exceeds 7mm, then the back trajectory point

before exceeding 7 mm rainfall is used as the source point. If it does not exceed 7mm, the 72-hour

665   point is used. More information on the analysis of air mass travel times over different surface types (land, open water, and ice) and the impact of precipitation (presuming > 7 mm cumulative rainfall can wash out aerosols in air mass by wet scavenging) can also be found in Wilbourn et al. (2024) and Gong et al. (2020).

ACKNOWLEDGMENTS:

670   This research was supported by the US Department of Energy, Office of Science, Office of Biological and Environmental Research (grant no. DE-SC-0018979). The authors gratefully acknowledge the NOAA Air Resources Laboratory (ARL) and Environmental Research Division's Data Access Program (ERDDAP) for the provision of the HYSPLIT transport and dispersion model and/or READY website (https://www.ready.noaa.gov) and the NOAA/PMEL ion

675   chromatography data used in this publication. A useful discussion regarding the ERDDAP data with NOAA's Lucia Upchurch and Patricia Quinn is also acknowledged. The authors acknowledge Valerie Sparks with Sandia National Labs for her onsite and administrative contributions to the ExINP-NSA campaign. Naruki Hiranuma, Aidan D. Pantoya, and Stephanie R. Simonsen thank Elise Wilbourn, Andebo A. Waza, Jacob Hurst, and Oyshrojo Talukder for their contribution to

680   the PINE-03 operation, maintenance, and error analysis. The authors also acknowledge Amy Solomon, Gourihar Kulkarni, and Matthew Shupe for useful discussion regarding the data implications. Gijs de Boer was supported by the US Department of Energy Atmospheric System Research (ASR) program under cooperative agreement DE-SC0013306, as well as by the NOAA Physical Sciences Laboratory. Christopher J. Cox received support from NOAA's Global Ocean

685   Monitoring and Observing Program through the Arctic Research Program (FundRef https://doi.org/10.13039/100018302) and the NOAA Physical Sciences Laboratory. Elisabeth Andrews was supported partly by the NOAA cooperative agreement with CIRES (NA17OAR4320101) and partly by the ARM user facility, a DOE Office of Science user facility managed by the Biological and Environmental Research program.

690   DATA AVAILABILITY:
The processed dataset and codes created for the study will be available at https://doi.org/10.6084/m9.figshare.26615752.v3 (Pantoya and Hiranuma, 2024). Local ambient conditions, such as wind speed, wind direction, temperature, and relative humidity, were obtained from NOAA-GML (https://gml.noaa.gov/aftp/data/meteorology/in-situ/brw/, last access: 10 June

695   2024). Visibility and time-averaged cumulative precipitation observations were not available at BRW for our study period and reported from Wiley Post-Will Rogers Memorial Airport (71.285° N, 156.769° W) (automated monitoring station; https://mesowest.utah.edu/cgi-bin/droman/download_api2.cgi?stn=PABR&hour1=03&min1=35&timetype=LOCAL&unit=0&graph=0, last access: 10 June 2024). Ion analysis data used for estimating ambient mass

700   concentrations of nss $SO_4^=$ and aerosol NO_3^- are available from NOAA-PMEL's website

(https://saga.pmel.noaa.gov/data/stations/, last access: 18 July 2024). Aerosol data from BRW are downloaded from NOAA-GML (https://gml.noaa.gov/aftp/aerosol/brw/, last access: 10 June 2024). The ARM CPC data is downloaded from ARM Data Discovery (doi: 10.5439/1227962). The scattering and aerosol size distribution data from El Arenosillo used to calculate Q was

705 downloaded from the EBAS data archive.

AUTHORS CONTRIBUTION:
NH designed the concept of this collaborative research. The methodology was developed by ADP, SRS, and NH. The onsite and remote measurements at the BRW site were conducted by BDT, RB, and ADP. The formal data analyses were led by ADP with the data processing contributions of SS,

710 EA, CJC, and GdB. ADP, SRS, and NH led the writing of the manuscript with the support of all authors.

COMPETING INTERESTS:
The authors declare no conflict of interest.

REFERENCES

REFERENCES

Andrews, E., Sheridan, P., Ogren, J. A., Hageman, D., Jefferson, A., Wendell, J., Alastuey, A., Alados-Arboledas, L., Bergin, M., Ealo, M., Hallar, A. G., Hoffer, A., Kalapov, I., Keywood, M., Kim, J., Kim, S.-W., Kolonjari, F., Labuschagne, C., Lin, N.-H., Macdonald, A., Mayol-Bracero, O. L., McCubbin, I. B., Pandolfi, M., Reisen, F., Sharma, S., Sherman, J. P., Sorribas, M., and Sun, J.: Overview of the NOAA/ESRL Federated Aerosol Network, B. Am. Meteorol. Soc., 100, 123–135, https://doi.org/10.1175/BAMS-D-17-0175.1, 2019.

Barr, S. L., Wyld, B., McQuaid, J. B., Neely III, R. R., and Murray, B. J.: Southern Alaska as a source of atmospheric mineral dust and ice-nucleating particles, Sci. Adv., 9, 3708, https://doi.org/10.1126/sciadv.adg3708, 2023.

Barrett, T. E., and Sheesley, R. J.: Year-round optical properties and source characterization of Arctic organic carbon aerosols on the North Slope Alaska, J. Geophys. Res. Atmos., 122, 9319–9331, https://doi.org/10.1002/2016JD026194, 2017.

Barry, K. R., Hill, T. C. J., Nieto-Caballero, M., Douglas, T. A., Kreidenweis, S. M., DeMott, P. J., and Creamean, J. M.: Active thermokarst regions contain rich sources of ice-nucleating particles, Atmos. Chem. Phys., 23, 15783–15793, https://doi.org/10.5194/acp-23-15783-2023, 2023.

Bond, T. C., Doherty, S. J., Fahey, D. W., Forster, P. M., Berntsen, T., DeAngelo, B. J., Flanner, M. G., Ghan, S., Kärcher, B., Koch, D., Kinne, S., Kondo, Y., Quinn, P. K., Sarofim, M. C., Schultz, M. G., Schulz, M., Venkataraman, C., Zhang, H., Zhang, S., Bellouin, N., Guttikunda, S. K., Hopke, P. K., Jacobson, M. Z., Kaiser, J. W., Klimont, Z., Lohmann, U., Schwarz, J. P., Shindell, D., Storelvmo, T., Warren, S. G., and Zender, C. S.: Bounding the role of black carbon in the climate system: A scientific assessment, J. Geophys. Res.-Atmos., 118, 5380–5552, https://doi.org/10.1002/jgrd.50171, 2013.

Chen, Q., Mirrielees, J. A., Thanekar, S., Loeb, N. A., Kirpes, R. M., Upchurch, L. M., Barget, A. J., Lata, N. N., Raso, A. R. W., McNamara, S. M., China, S., Quinn, P. K., Ault, A. P., Kennedy, A., Shepson, P. B., Fuentes, J. D., and Pratt, K. A.: Atmospheric particle abundance and sea salt aerosol observations in the springtime Arctic: a focus on blowing snow and leads, Atmos. Chem. Phys., 22, 15263–15285, https://doi.org/10.5194/acp-22-15263-2022, 2022.

Cox, C. J., Stone, R. S., Douglas, D. C., Stanitski, D. M., and Gallagher, M. R.: The Aleutian Low-Beaufort Sea Anticyclone: A climate index correlated with the timing of springtime melt in the Pacific Arctic cryosphere. Geophysical Research Letters, 46, 7464–7473, https://doi.org/10.1029/2019GL083306, 2019.

Cox, C. J., Stone, R. S., Douglas, D. C., Stanitski, D. M., Divoky, G. J., Dutton, G. S., Sweeney, C., George, J. C., and Longenecker, D. U.: Drivers and environmental responses to the changing annual snow cycle of northern Alaska, B. Am. Meteorol. Soc., 98, 2559–2577, https://doi.org/10.1175/BAMS-D-16-0201.1, 2017.

Cox, C. J., Walden, V. P., and Rowe, P. M.: A comparison of the atmospheric conditions at Eureka, Canada, and Barrow, Alaska (2006–2008), J. Geophys. Res., 117, D12204, https://doi.org/10.1029/2011JD017164, 2012.

Creamean, J. M., Barry, K., Hill, T. C. J., Hume, C., DeMott, P. J., Shupe, M. D., Dahlke, S., Willmes, S., Schmale, J., Beck, I., Hoppe, C. J. M., Fong, A., Chamberlain, E., Bowman, J., Scharien, R., and Persson, O.: Annual cycle observations of aerosols capable of ice

formation in central Arctic clouds, Nat. Commun., 13, 3537, https://doi.org/10.1038/s41467-022-31182-x, 2022.

Creamean, J. M., Cross, J. N., Pickart, R., McRaven, L., Lin, P., Pacini, A., Hanlon, R., Schmale, D. G., Ceniceros, J., Aydell, T., Colombi, N., Bolger, E., and DeMott, P. J.: Ice Nucleating Particles Carried From Below a Phytoplankton Bloom to the Arctic Atmosphere, Geophys. Res. Lett., 46, 8572–8581, https://doi.org/10.1029/2019GL083039, 2019.

Creamean, J. M., Maahn, M., de Boer, G., McComiskey, A., Sedlacek, A. J., and Feng, Y.: The influence of local oil exploration and regional wildfires on summer 2015 aerosol over the North Slope of Alaska, Atmos. Chem. Phys., 18, 555–570, https://doi.org/10.5194/acp-18-555-2018, 2018a.

Creamean, J. M., Kirpes, R. M., Pratt, K. A., Spada, N. J., Maahn, M., de Boer, G., Schnell, R. C., and China, S.: Marine and terrestrial influences on ice nucleating particles during continuous springtime measurements in an Arctic oilfield location, Atmos. Chem. Phys., 18, 18023–18042, https://doi.org/10.5194/acp-18-18023-2018, 2018b.

de Boer, G., Cox, C.J., and Creamean, J. M.: Accelerated springtime melt of northern Alaska river systems resulting from niveo-aeolian deposition events, Arctic, 72, 215–335, https://doi.org/10.14430/arctic68654, 2019.

Delene, D. J., and Ogren, J. A.: Variability of aerosol optical properties at four North American surface monitoring sites. J. Atmos. Sci., 59, 1135–1150, https://doi.org/10.1175/1520-0469(2002)059<1135:VOAOPA>2.0.CO;2, 2002.

DeMott, P. J., Hill, T. C., McCluskey, C. S., Prather, K. A., Collins, D. B., Sullivan, R. C., Ruppel, M. J., Mason, R. H., Irish, V. E., Lee, T., Hwang, C. Y., Rhee, T. S., Snider, J. R., McMeeking, G. R., Dhaniyala, S., Lewis, E. R., Wentzell, J. J., Abbatt, J., Lee, C., Sultana, C. M., Ault, A. P., Axson, J. L., Diaz Martinez, M., Venero, I., Santos-Figueroa, G., Stokes, M. D., Deane, G. B., Mayol-Bracero, O. L., Grassian, V. H., Bertram, T. H., Bertram, A. K., Moffett, B. F., and Franc, G. D.: Sea spray aerosol as a unique source of ice nucleating particles, P. Natl. Acad. Sci. USA, 113, 5797–5803, https://doi.org/10.1073/pnas.1514034112, 2016.

Fetterer, F., Knowles, K., Meier, W. N., Savoie, M., and Windnagel, A. K.: Sea Ice Index, Version 3 [Sea Ice Extent]. Boulder, Colorado USA. National Snow and Ice Data Center. https://doi.org/10.7265/N5K072F8, 2017.

Fountain, A. G. and Ohtake, T.: Concentrations and Source Areas of Ice Nuclei in the Alaskan Atmosphere, J. Clim. Appl. Meteorol., 24, 377–382, https://doi.org/10.1175/1520-0450(1985)024<0377:Casaoi>2.0.CO;2, 1985.

Gong, X., Wex, H., Voigtländer, J., Fomba, K. W., Weinhold, K., van Pinxteren, M., Henning, S., Müller, T., Herrmann, H., and Stratmann, F.: Characterization of aerosol particles at Cabo Verde close to sea level and at the cloud level – Part 1: Particle number size distribution, cloud condensation nuclei and their origins, Atmos. Chem. Phys., 20, 1431–1449, https://doi.org/10.5194/acp-20-1431-2020, 2020.

Hande, L. B. and Hoose, C.: Partitioning the primary ice formation modes in large eddy simulations of mixed-phase clouds, Atmos. Chem. Phys., 17, 14105–14118, https://doi.org/10.5194/acp-17-14105-2017, 2017.

Hoose, C. and Möhler, O.: Heterogeneous ice nucleation on atmospheric aerosols: a review of results from laboratory experiments, Atmos. Chem. Phys., 12, 9817–9854, https://doi.org/10.5194/acp-12-9817-2012, 2012.

Inoue, J., Tobo, Y., Taketani, F., and Sato, K.: Oceanic supply of ice-nucleating particles and its effect on ice cloud formation: A case study in the Arctic ocean during a cold-air outbreak in early winter, Geophys. Res. Lett., 48, e2021GL094646, https://doi.org/10.1029/2021GL094646, 2021.

Irish, V. E., Hanna, S. J., Willis, M. D., China, S., Thomas, J. L., Wentzell, J. J. B., Cirisan, A., Si, M., Leaitch, W. R., Murphy, J. G., Abbatt, J. P. D., Laskin, A., Girard, E., and Bertram, A. K.: Ice nucleating particles in the marine boundary layer in the Canadian Arctic during summer 2014, Atmos. Chem. Phys., 19, 1027–1039, https://doi.org/10.5194/acp-19-1027-2019, 2019a.

Irish, V. E., Hanna, S. J., Xi, Y., Boyer, M., Polishchuk, E., Ahmed, M., Chen, J., Abbatt, J. P. D., Gosselin, M., Chang, R., Miller, L. A., and Bertram, A. K.: Revisiting properties and concentrations of ice-nucleating particles in the sea surface microlayer and bulk seawater in the Canadian Arctic during summer, Atmos. Chem. Phys., 19, 7775–7787, https://doi.org/10.5194/acp-19-7775-2019, 2019b.

Kanji, Z. A., Ladino, L. A., Wex, H., Boose, Y., Burkert-Kohn, M., Cziczo, D. J., and Kramer, M.: Overview of Ice Nucleating Particles. In D. Baumgardner, G. M. McFarquhar, & A. J. Heymsfield (Eds.), Ice Formation and Evolution in Clouds and Precipitation: Measurement and Modeling Challenges, Meteorological Monographs, 58, 1.1-1.33. https://doi.org/10.1175/amsmonographs-d-16-0006.1, 2017.

Kolesar, K. R., Cellini, J., Peterson, P. K., Jefferson, A., Tuch, T., Birmili, W., Wiedensohler, A., and Pratt, K. A.: Effect of Prudhoe Bay emissions on atmospheric aerosol growth events observed in Utqiagvik (Barrow), Alaska, Atmos. Environ., 152, 146–155, https://doi.org/10.1016/j.atmosenv.2016.12.019, 2017.

Keene, W. C., Pszenny, A. A. P., Galloway, J. N., and Hawley, M. E.: Sea-salt corrections and interpretation of constituent ratios in marine precipitation, J. Geophys. Res., 91D, 6647–6658, 1986.

Knopf, D. A., Barry, K. R., Brubaker, T. A., Jahl, L. G., Jankowski, K. A., Li, J., Lu, Y., Monroe, L. W., Moore, K. A., Rivera-Adorno, F. A., Sauceda, K. A., Shi, Y., Tomlin, J. M., Vepuri, H. S. K., Wang, P., Lata, N. N., Levin, E. J. T., Creamean, J. M., Hill, T. C. J., China, S., Alpert, P. A., Moffet, R. C., Hiranuma, N., Sullivan, R. C., Fridlind, A. M., West, M., Riemer, N., Laskin, A., DeMott, P. J., and Liu, X.: Aerosol-ice formation closure: A Southern Great Plains field campaign, B. Am. Meteorol. Soc., 102, E1952–E1971, https://doi.org/10.1175/Bams-D-20-0151.1, 2021.

Koop, T. and Murray, B. J.: A physically constrained classical description of the homogeneous nucleation of ice in water, J. Chem. Phys., 145, 211915, https://doi.org/10.1063/1.4962355, 2016.

Lacher, L., Adams, M. P., Barry, K., Bertozzi, B., Bingemer, H., Boffo, C., Bras, Y., Büttner, N., Castarede, D., Cziczo, D. J., DeMott, P. J., Fösig, R., Goodell, M., Höhler, K., Hill, T. C. J., Jentzsch, C., Ladino, L. A., Levin, E. J. T., Mertes, S., Möhler, O., Moore, K. A., Murray, B. J., Nadolny, J., Pfeuffer, T., Picard, D., Ramírez-Romero, C., Ribeiro, M., Richter, S., Schrod, J., Sellegri, K., Stratmann, F., Swanson, B. E., Thomson, E. S., Wex, H., Wolf, M. J., and Freney, E.: The Puy de Dôme ICe Nucleation Intercomparison Campaign (PICNIC): comparison between online and offline methods in ambient air, Atmos. Chem. Phys., 24, 2651–2678, https://doi.org/10.5194/acp-24-2651-2024, 2024.

Lee, J., Seifert, P., Hashino, T., Maahn, M., Senf, F., and Knoth, O.: Numerical evidence that the impact of CCN and INP concentrations on mixed-phase clouds is observable with cloud radars, EGUsphere [preprint], https://doi.org/10.5194/egusphere-2023-1887, 2023.

Li, G., Wieder, J., Pasquier, J. T., Henneberger, J., and Kanji, Z. A.: Predicting atmospheric background number concentration of ice-nucleating particles in the Arctic, Atmos. Chem. Phys., 22, 14441–14454, https://doi.org/10.5194/acp-22-14441-2022, 2022.

Mamouri, R.-E. and Ansmann, A.: Potential of polarization lidar to provide profiles of CCN- and INP-relevant aerosol parameters, Atmos. Chem. Phys., 16, 5905–5931, https://doi.org/10.5194/acp-16-5905-2016, 2016.

Mason, R. H., Si, M., Chou, C., Irish, V. E., Dickie, R., Elizondo, P., Wong, R., Brintnell, M., Elsasser, M., Lassar, W. M., Pierce, K. M., Leaitch, W. R., MacDonald, A. M., Platt, A., Toom-Sauntry, D., Sarda-Estève, R., Schiller, C. L., Suski, K. J., Hill, T. C. J., Abbatt, J. P. D., Huffman, J. A., DeMott, P. J., and Bertram, A. K.: Size-resolved measurements of ice-nucleating particles at six locations in North America and one in Europe, Atmos. Chem. Phys., 16, 1637–1651, https://doi.org/10.5194/acp-16-1637-2016, 2016.

McCluskey, C. S., Ovadnevaite, J., Rinaldi, M., Atkinson, J., Belosi, F., Ceburnis, D., Marullo, S., Hill, T. C. J., Lohmann, U., Kanji, Z. A., O'Dowd, C., Kreidenweis, S. M., and DeMott, P. J.: Marine and Terrestrial Organic Ice-Nucleating Particles in Pristine Marine to Continentally Influenced Northeast Atlantic Air Masses, J. Geophys. Res., 123, 6196–6212, https://doi.org/10.1029/2017JD028033, 2018.

Moffett, C. E., Mehra, M., Barrett, T. E., Gunsch, M. J., Pratt, K. A., and Sheesley, R. J.: Contemporary sources dominate carbonaceous aerosol on the North Slope of Alaska. Sci. Total Environ. **2022**, 831, 154641, https://doi.org/10.1016/j.scitotenv.2022.154641, 2022.

Möhler, O., Adams, M., Lacher, L., Vogel, F., Nadolny, J., Ullrich, R., Boffo, C., Pfeuffer, T., Hobl, A., Weiß, M., Vepuri, H. S. K., Hiranuma, N., and Murray, B. J.: The Portable Ice Nucleation Experiment (PINE): a new online instrument for laboratory studies and automated long-term field observations of ice-nucleating particles, Atmos. Meas. Tech., 14, 1143–1166, https://doi.org/10.5194/amt-14-1143-2021, 2021.

Moore, K. A., Alexander, S. P., Humphries, R. S., Jensen, J., Protat, A., Reeves, J. M., Sanchez, K. J., Kreidenweis, S. M., and DeMott, P. J.: Estimation of sea spray aerosol surface area over the Southern Ocean using scattering measurements, J. Geophys. Res.-Atmos., 127, e2022JD037009, https://doi.org/10.1029/2022JD037009, 2022.

Morrison, H., de Boer, G., Feingold, G., Harrington, J., Shupe, M. D., and Sulia, K.: Resilience of persistent Arctic mixed-phase clouds, Nat. Geosci., 5, 11–17, https://doi.org/10.1038/ngeo1332, 2012.

Murray, B. J., Carslaw, K. S., and Field, P. R.: Opinion: Cloud-phase climate feedback and the importance of ice-nucleating particles, Atmos. Chem. Phys., 21, 665–679, https://doi.org/10.5194/acp-21-665-2021, 2021.

Ogren, J. A., Wendell, J., Andrews, E., and Sheridan, P. J.: Continuous light absorption photometer for long-term studies, Atmos. Meas. Tech., 10, 4805–4818, https://doi.org/10.5194/amt-10-4805-2017, 2017.

Pantoya, A. D., and Hiranuma, N.: The abundance of ground-level atmospheric ice-nucleating particles and aerosol properties in the North Slope of Alaska. figshare. Dataset, Ffgshare, https://doi.org/10.6084/m9.figshare.26615752.v3, 2024.

Polissar, A. V., Hopke, P. K., Paatero, P., Kaufmann, Y. J., Hall, D. K., Bodhaine, B. A., Dutton, E. G., and Harris, J. M.: The aerosol at Barrow, Alaska: long-term trends and source

locations, Atmos. Environ., 33, 2441–2458, https://doi.org/10.1016/S1352-2310(98)00423-3, 1999.

Prenni, A. J., Harrington, J. Y., Tjernstrom, M., DeMott, P. J., Avramov, A., Long, C. N., Kreidenweis, S. M., Olsson, P. Q., and Verlinde, J.: Can ice-nucleating aerosols affect Arctic seasonal climate?, B. Am. Meteorol. Soc., 88, 541–550, https://doi.org/10.1175/bams-88-4-541, 2007.

Quinn, P. K., Shaw, G., Andrews, E., Dutton, E. G., Ruoho-Airola, T., and Gong, S. L.: Arctic haze: current trends and knowledge gaps, Tellus B, 59, 99–114, https://doi.org/10.1111/j.1600-0889.2006.00238.x, 2007.

Quinn, P. K., Miller, T. L., Bates, T. S., Ogren, J. A., Andrews, E., and Shaw, G. E.: A 3-year record of simultaneously measured aerosol chemical and optical properties at Barrow, Alaska, J. Geophys. Res., 107, https://doi.org/10.1029/2001JD001248, 2002.

Quinn, P. K., Bates, T. S., Miller, T. L., Coffman, D. J., Johnson, J. E., Harris, J. M., Ogren, J. A., Forbes, G., Anderson, T. L., Covert, D. S., and Rood, M. J.: Surface submicron aerosol chemical composition: What fraction is not sulfate?, J. Geophys. Res., 105, 6785–6806, https://doi.org/10.1029/1999JD901034, 2000.

Quinn, P., Coffman, D., Kapustin, V., Bates, V., and Covert, D.: Aerosol optical properties in the marine boundary layer during the First Aerosol Characterization Experiment (ACE 1) and the underlying chemical and physical aerosol properties, J. Geophys. Res.-Atmos., 103, 16547–16563, https://doi.org/10.1029/97JD02345, 1998.

Rogers, D. C., DeMott, P. J., Kreidenweis, S. M., and Chen, Y.: A continuous-flow diffusion chamber for airborne measurements of ice nuclei, J. Atmos. Oceanic Technol., **18**, 725–741, https://doi.org/10.1175/1520-0426(2001)018<0725:ACFDCF>2.0.CO;2, 2001.

Rolph, G., Stein, A., and Stunder, B.: Real-time Environmental Applications and Display sYstem: READY, Environ. Model. Softw., 95, 210–228, https://doi.org/10.1016/j.envsoft.2017.06.025, 2017.

Sanchez-Marroquin, A., Barr, S. L., Burke, I. T., McQuaid, J. B., and Murray, B. J.: Aircraft ice-nucleating particle and aerosol composition measurements in the western North American Arctic, Atmos. Chem. Phys., 23, 13819–13834, https://doi.org/10.5194/acp-23-13819-2023, 2023.

Sanchez-Marroquin, A., Arnalds, O., Baustian-Dorsi, K. J., Browse, J., Dagsson-Waldhauserova, P., Harrison, A. D., Maters, E. C., Pringle, K. J., Vergara-Temprado, J., Burke, I. T., McQuaid, J. B., Carslaw, K. S., and Murray, B. J.: Iceland is an episodic source of atmospheric ice-nucleating particles relevant for mixed-phase clouds, Sci. Adva., 6, eaba8137, https://doi.org/10.1126/sciadv.aba8137, 2020.

Schmeisser, L., Backman, J., Ogren, J. A., Andrews, E., Asmi, E., Starkweather, S., Uttal, T., Fiebig, M., Sharma, S., Eleftheriadis, K., Vratolis, S., Bergin, M., Tunved, P., and Jefferson, A.: Seasonality of aerosol optical properties in the Arctic, Atmos. Chem. Phys., 18, 11599–11622, https://doi.org/10.5194/acp-18-11599-2018, 2018.

Sheridan, P., Andrews, E., Schmeisser, L., Vasel, B., and Ogren, J.: Aerosol Measurements at South Pole: Climatology and Impact of Local Contamination, Aerosol Air Qual. Res., 16, 855–872, https://doi.org/10.4209/aaqr.2015.05.0358, 2016.

Shupe, M. D., and Intrieri, J. M.: Cloud radiative forcing of the Arctic surface: the influence of cloud properties, surface albedo, and solar zenith angle. J. Climate, **17**, 616–628, https://doi.org/10.1175/1520-0442(2004)017<0616:CRFOTA>2.0.CO;2, 2004.

Shupe, M. D., Persson, P. O. G., Brooks, I. M., Tjernström, M., Sedlar, J., Mauritsen, T., Sjogren, S., and Leck, C.: Cloud and boundary layer interactions over the Arctic sea ice in late summer, Atmos. Chem. Phys., 13, 9379–9399, https://doi.org/10.5194/acp-13-9379-2013, 2013.

Shupe, M. D.: Clouds at Arctic Atmospheric Observatories. Part II: Thermodynamic Phase Characteristics, J. Appl. Meteorol. Climatol., 50, 645–661, https://doi.org/10.1175/2010jamc2468.1, 2011.

Shupe, M. D., Walden, V. P., Eloranta, E., Uttal, T., Campbell, J. R., Starkweather, S. M., and Shiobara, M.: Clouds at Arctic Atmospheric Observatories. Part I: Occurrence and Macrophysical Properties, J. Appl. Meteorol. Climatol., 50, 626–644, https://doi.org/10.1175/2010jamc2467.1, 2010.

Solomon, A., de Boer, G., Creamean, J. M., McComiskey, A., Shupe, M. D., Maahn, M., and Cox, C.: The relative impact of cloud condensation nuclei and ice nucleating particle concentrations on phase partitioning in Arctic mixed-phase stratocumulus clouds, Atmos. Chem. Phys., 18, 17047–17059, https://doi.org/10.5194/acp-18-17047-2018, 2018.

Solomon, A., Morrison, H., Persson, O., Shupe, M., and Bao, J.-W.: Investigations of microphysical parameterizations of snow and ice in Arctic clouds during M-PACE through model-observations comparison, Mon. Wea. Rev., 137, 3110–3128, 2009.

Stein, A. F., Draxler, R. R., Rolph, G. D., Stunder, B. J. B., Cohen, M. D., and Ngan, F.: Noaa's Hysplit atmospheric transport and dispersion modeling system, B. Am. Meteorol. Soc., 96, 2059–2077, https://doi.org/10.1175/Bams-D-14-00110.1, 2015.

Ullrich, R., Hoose, C., Möhler, O., Niemand, M., Wagner, R., Höhler, K., Hiranuma, N., Saathoff, H., and Leisner, T.: A New Ice Nucleation Active Site Parameterization for Desert Dust and Soot, J. Atmos. Sci., 74, 699–717, https://doi.org/10.1175/JAS-D-16-0074.1, 2017.

Vali, G., DeMott, P. J., Möhler, O., and Whale, T. F.: Technical Note: A proposal for ice nucleation terminology, Atmos. Chem. Phys., 15, 10263–10270, https://doi.org/10.5194/acp-15-10263-2015, 2015.

Welti, A., Bigg, E. K., DeMott, P. J., Gong, X., Hartmann, M., Harvey, M., Henning, S., Herenz, P., Hill, T. C. J., Hornblow, B., Leck, C., Löffler, M., McCluskey, C. S., Rauker, A. M., Schmale, J., Tatzelt, C., van Pinxteren, M., and Stratmann, F.: Ship-based measurements of ice nuclei concentrations over the Arctic, Atlantic, Pacific and Southern oceans, Atmos. Chem. Phys., 20, 15191–15206, https://doi.org/10.5194/acp-20-15191-2020, 2020.

Westbrook, C. D. and Illingworth, A. J.: Evidence that ice forms primarily in supercooled liquid clouds at temperatures $> -27\,°C$, Geophys. Res. Lett., 38, L14808, https://doi.org/10.1029/2011gl048021, 2011.

Wilbourn, E. K., Lacher, L., Guerrero, C., Vepuri, H. S. K., Höhler, K., Nadolny, J., Pantoya, A. D., Möhler, O., and Hiranuma, N.: Measurement report: A comparison of ground-level ice-nucleating-particle abundance and aerosol properties during autumn at contrasting marine and terrestrial locations, Atmos. Chem. Phys., 24, 5433–5456, https://doi.org/10.5194/acp-24-5433-2024, 2024.

Wilbourn, E. K., Alrimaly, S., Williams, H., Hurst, J., McGovern, G. P., Anderson, T. A., and Hiranuma, N.: Integrated science teaching in atmospheric ice nucleation research: Immersion freezing experiments, J. Chem. Educ., 100, 1511–1522, https://doi.org/10.1021/acs.jchemed.2c01060, 2023.

Zheng, G., Wang, Y., Aiken, A. C., Gallo, F., Jensen, M. P., Kollias, P., Kuang, C., Luke, E., Springston, S., Uin, J., Wood, R., and Wang, J.: Marine boundary layer aerosol in the

eastern North Atlantic: seasonal variations and key controlling processes, Atmos. Chem. Phys., 18, 17615–17635, https://doi.org/10.5194/acp-18-17615-2018, 2018.